ANGULAR TRAPPING OF A MIRROR USING RADIATION PRESSURE

By

David B. Kelley

B.S. Massachusetts Institute of Technology, Cambridge, MA, 2010
M.S. Syracuse University, Syracuse, NY, 2013

Dissertation
Submitted in Partial Fulfillment of the Requirements
for the degree of
Doctor of Philosophy in Physics

Syracuse University
September 2015

ANGULAR TRAPPING OF A MIRROR USING RADIATION PRESSURE

By

David B. Kelley

B.S. Massachusetts Institute of Technology, Cambridge, MA, 2010
M.S. Syracuse University, Syracuse, NY, 2013

Dissertation
Submitted in Partial Fulfillment of the Requirements
for the degree of
Doctor of Philosophy in Physics

Syracuse University
September 2015

Approved : _____
Prof. Stefan Ballmer

Date : _____

ABSTRACT

Alignment control in gravitational-wave detectors has consistently proven to be a difficult problem due to the stringent noise contamination requirement for the gravitational wave readout and the radiation-pressure induced angular instability in Fabry-Perot cavities (Sidles-Sigg instability). I present the development, implementation, and measurement of a dual-carrier control scheme which uses radiation pressure to control a suspended mirror, trapping it in the longitudinal degree of freedom and one angular degree of freedom.

Contents

List of Tables

List of Figures

Preface

The work presented in this thesis stems from my participation in the LIGO Scientific Collaboration (LSC). This work does not reflect the scientific opinion of the LSC and it was not reviewed by the collaboration.

The theory of optical trapping in two degrees of freedom in chapter 1 is based on

A. Perreca *et al.*, "Multi-dimensional optical trapping of a mirror," *Phys. Rev. D* **89** (2014) 122002.

Chapter 4 is based on material from

David B. Kelley *et al.*, "Observation of photo-thermal feed-back in a stable dual-carrier optical spring," to be submitted to *Phys. Rev. D*.

Chapter 5 is based on

David B. Kelley *et al.*, "Angular Trap Demonstration," to be submitted to *Phys. Rev. D*

Acknowledgments

Thanks for the music.....

to

my parents and Emma

Chapter 1

Introduction

The Advanced Laser Interferometer Gravitational-Wave Observatory (aLIGO) is part of an international effort to detect gravitational waves. The search will resume later this year with the two aLIGO sites in Washington and Louisiana, which will ramp up to full design sensitivity over the following few years.

One of the remaining improvements is to increase the input power from about 25 watts to 125 watts. One effect that will scale with power is the Sidles-Sigg instability. This effect must be dealt with by using active controls on the angular degrees of freedom of the test masses.

1.1 Basic layout of aLIGO

Michelson with Fabry-Perot arms

1.2 Optical Springs

What is an optical spring?

How do you make one?

Useful characteristics of optical springs?

Chapter 2

Suspensions

Suspending the optics is one of the most complicated parts of the experiment. The optics are constructed as discs with roughly 76 mm (3 inch) diameters. They are suspended from modified Small Optics Suspensions (SOSs) and controlled with Optical Sensing Electro-Magnets (OSEMs).

2.1 Input coupler

The input coupler (see fig 1) is designed to hold three mirrors at specific positions and angles. The design concerns governing the placement of the holes include the separation of the beams, the angle of the folded cavity, and the desired lengths of the two cavities.

2.2 End mirror

The end mirror is hung from a steel ring by three glass fibers.

pictured in 24

2.3 Blade Springs

This is a discussion of the relevant physics to the construction of blade spring suspensions for a small optics suspension.

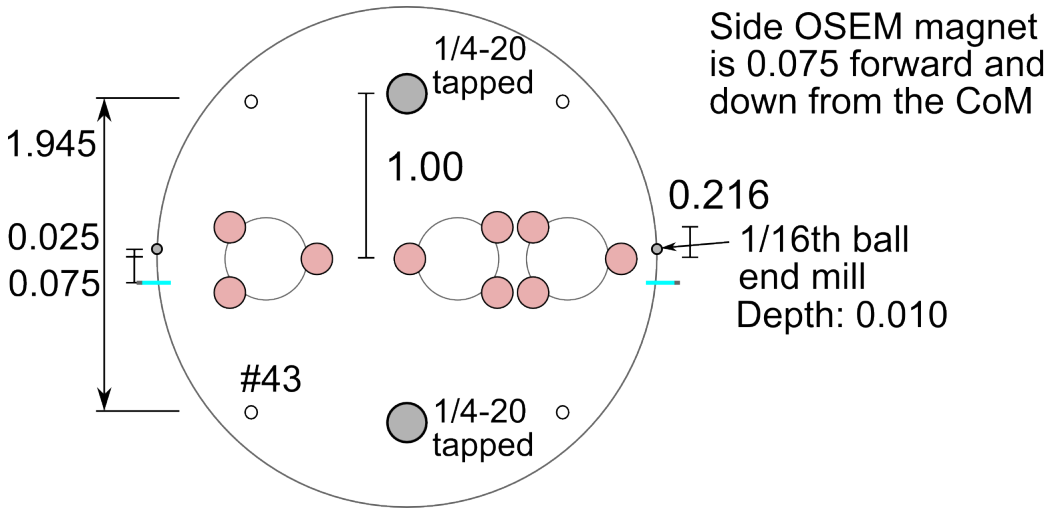

Figure 1 : The input coupler for the cavity.

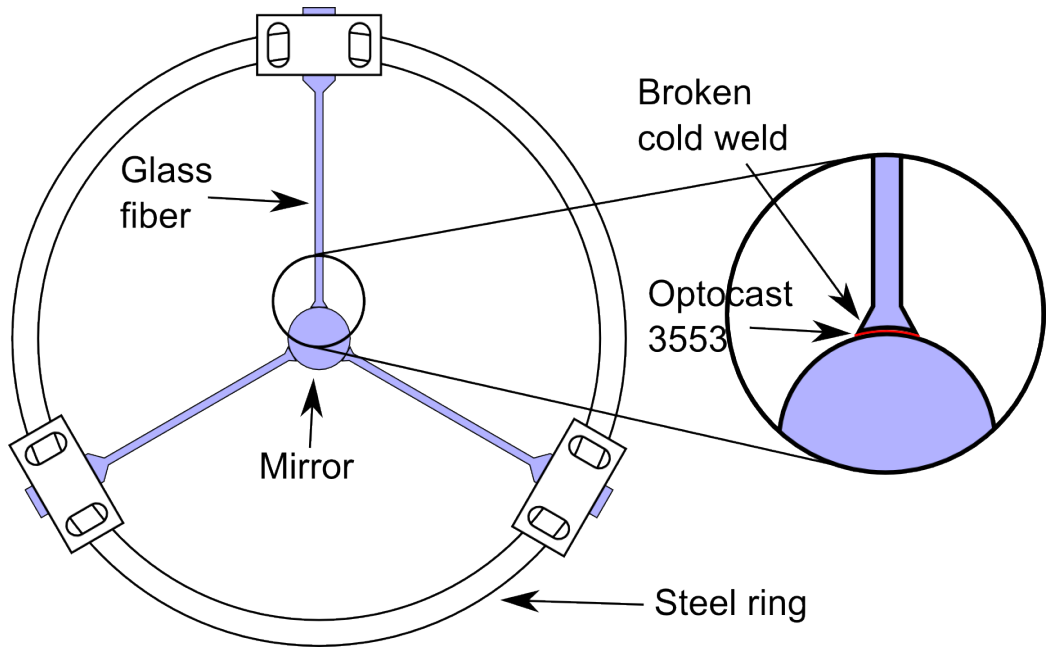

Figure 2 : End mass suspension.

This theoretical parts of the paper are based primarily on the notes posted in the DCC [1].

2.3.1 A little theory

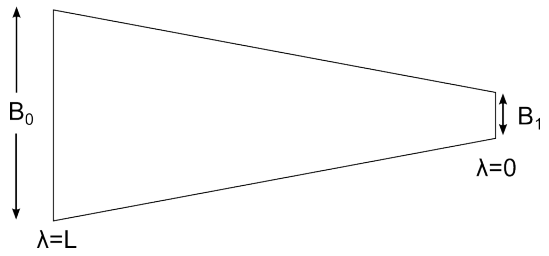

Figure 3 : Profile drawing of a deflected blade spring. R is the radius of the circle described by the blade spring when it is under stress. L is the length of the blade, b_0 is the large base and b_1 is the small base. λ is the distance along the blade

The paper gives the general formula for an elastic beam under a load (see Rourke's formulas for stress and strain, eq. 8.1-4):

$$\frac{E}{R(\lambda)} = \frac{M(\lambda)}{I(\lambda)} \tag{2.1}$$

Here λ is the distance along the blade (with the $\lambda = 0$ at the tip), E is the Young's modulus, R is the radius of curvature at λ, I is the area moment of inertia at λ, and M is the bending moment at λ, expressed as:

$$M = mg\lambda \tag{2.2}$$

where m is mass supported, g is $9.81\mathrm{m/s}^2$.

$b = b_1 + (b_0 - b_1)\frac{\lambda}{L}$ is the width between $\lambda = 0$ ($b = b_1$) and $\lambda = L$ ($b = b_0$) (see figure 3) so

$$I = \frac{bt^3}{12} = (b_0 - b_1)\frac{t^3}{12}\frac{\lambda}{L} + b_1\frac{t^3}{12} \tag{2.3}$$

where t is the thickness of the blade and L is the blade length. If we consider the blade to be triangular ($b_1 = 0$), I becomes

[1] https://dcc.ligo.org/LIGO-T030285

$$I = \frac{b_0 t^3}{12}\frac{\lambda}{L} \tag{2.4}$$

Then we see that

$$\frac{E}{R(\lambda)} = \frac{M(\lambda)}{I(\lambda)} = \frac{mg\lambda}{b_0 \frac{t^3}{12}\frac{\lambda}{L}} = \frac{12mgL}{b_0 t^3} \quad \rightarrow \quad R = constant \tag{2.5}$$

In other words, R is constant along the blade (the blade profile is circular). We can accomplish this behavior by specifying that the wire is clamped where the end of the 'triangle' should be. You may have noticed that the calculation is based on an initially flat beam. We attempted to add a cosine term to account for the monting angle, but the predictions were inaccurate.

Thus we can, without difficulty, treat a change in force on the spring (for instance by changing the mass) as a change in the radius of curvature of the blade.

From eq.2.5 we obtain R

$$R(\lambda) = R = \frac{Eb_0 t^3}{12mgL} \tag{2.6}$$

From eq.2.6 we can obtain the bounce mode frequency f_b

$$f_b = \frac{1}{2\pi}\sqrt{\frac{Eb_0 t^3}{6mL^3}} \tag{2.7}$$

and the stress in the blade as:

$$\sigma = \frac{6mgL}{b_0 t^2}; \tag{2.8}$$

We can use equation 2.8, solved for b_0, to simplify equation 2.7, thus

$$f_b = \frac{1}{2\pi}\sqrt{\frac{Egt}{L^2\sigma}} \tag{2.9}$$

Given a target stress σ, a target bounce frequency f_b, and a length limit L based on the chamber dimensions, we can determine the proper thickness t for the blade.

If we manipulate equations 2.9 and 2.8, we get

$$t = \frac{(2pif_bL)^2\sigma}{Eg} = \sqrt{\frac{6mgL}{b_0\sigma}} \tag{2.10}$$

This equation gives the minimum requirement to make a blade spring.

2.3.2 Materials

The LIGO-recommended material is "maraging" steel (sometimes known by the trade-name Vascomax), which is easy to machine, but becomes incredibly hard when baked. One drawback of this material is that it can corrode over time. To combat this, LIGO recommends putting a nickel plating on the blades [2]. The hardness of the final product is the primary reason it is used. This material is difficult and expensive (best offer was $1200 for six blade's worth) to buy in small quantities.

As an alternative, we are considering "full hardened" 301 stainless steel. It is a factor of about 2.5 weaker than the maraging steel, but we have have found that workable solutions exist.

A third alternative is 17-4 precipitation hardened (PH) stainless. This material is similar to maraging steel in that it becomes harder when you bake it. Baking at 900 F for one hour results in a yield strength of 200000 psi = 1379 MPa. Baking longer or at a higher temperature makes the material a bit sorfter, but this behavior is understood and fairly error-tolerant [3]

One more alternative which LIGO uses for the small blade springs is 304 stainless (yield strength of 200 MPa) because the expected strain in the small blades is about 80 MPa.

For comparison, McMaster has details of many of the metals that are available [4]. All of the metals we are considering are on the LIGO vacuum compatible materials list[5].

When we are determining the maximum amount of stress that the blade can withstand before deforming, we typically use the yield strength. This is the amount

[2] https://dcc.ligo.org/LIGO-E0900023

[3] http://www.aksteel.com/pdf/markets_products/stainless/precipitation/17-4_PH_Data_Bulletin.pdf

[4] http://www.mcmaster.com/library/20121105/8984KAC.pdf

[5] https://dcc.ligo.org/LIGO-E960050

of stress that causes the metal to deform by 0.2%. We have chosen as a target strain 60% of the yield strength.

One LIGO document [6] adds a factor related to the Poisson's Ratio to the Young's Modulus which effectively increases the strain. This is attributed to a change in the strain of the material due to bending. Our predictions seem to work better with this factor removed, but we have chosen to keep the factor for the moment because it represents the 'worst case' scenerio.

Steel	E (GPa)	E (psi)	σ_{max} (MPa)	σ_{max} (PSI)
C350 Maraging	200	29×10^6	2344	34×10^4
301 Stainless	193	28×10^6	965	14×10^4
17-4 PH Stainless	196.5	28.5×10^6	1379	20×10^4
304 Stainless	193	28×10^6	207	3×10^4

Table 1 : Characteristics of proposed materials.

2.3.3 Blade spring design

Criteria for the design following the section 2.3.1:

1. Maintain safe levels $\leq 80\%$ of material stress limits: $\sigma \leq 0.8\sigma_{max}$.
2. All parts must fit within the area of the 27 inch diameter top plate in the bell jar. The length L of the blade springs is fixed at 19"; when under load the bending will reduce the effective length.
3. Choose a 'small' (within reason) bounce mode frequency (This determines t).
4. Minimize vertical to horizontal coupling, looking at the effective length z_{max} as a function of different loads and angles. We could adjust the weight for a given angle or at fixed weight we adjust the angle. The latter is our way to go.

Using equations from 2.6 to 2.10 we have found parameters that satisfy the criteria. We are using 17-4 stainless steel. The maximum stress of this design is only 60% of the expected yield strength of the material. This gives us more leeway with the construction and reduces the chance of failure sue to improper baking.

[6] https://dcc.ligo.org/LIGO-T0900324

2.3.4 Small blade

At the same time, we are designing a similar suspension to be mounted on top of each SOS. These will be much smaller, but will follow the same design principles.

For the small spring system, our design is very similar to the parameters used in the HAM AUX design for ALIGO [7] We can use 304 Stainless or 17-4 Stainless with little impact on the final performance. The maximum stress of this design is only 40% of the expected yield strength of 304 and much less than that for 17-4. This gives us more leeway with the construction and reduces the chance of failure due to improper baking. The final design schematic is shown in figure 5. For the small design we have chosen to neglect the Poisson Ratio factor because the bending is much smaller. We are motivated to do this by the HAM AUX design mentioned earlier.

2.3.5 Small springs

Parameter	**Metric**	**Imperial**
Blade length, L	7.68 cm	3.0 in
Blade base width, b_0	3.3 cm	1.3 in
Blade thickness, t	0.51 mm	0.020 in
Mounting angle, θ	0.083 rad	4.78°
Supported mass, m	0.15 kg	0.33 lbs
Result	**Metric**	**Imperial**
Bounce Frequency, f_b	7.19 Hz	
Max height	2 mm	0.08 in
Tip height	2 mm	0.06 in
Effective length	7.7 cm	3.0 in
Maximum Stress, σ	81 MPa	11700 PSI

Table 2 : Characteristics of proposed blade design

[7] https://dcc.ligo.org/LIGO-T1000339

2.3.6 Coupling

For the small spring system, we do not need to worry about this coupling because the motion will not couple to the position degree of freedom. We should note that changing the effective length would result in a change in the yaw mode resonance of the suspended structure, which may be an issue.

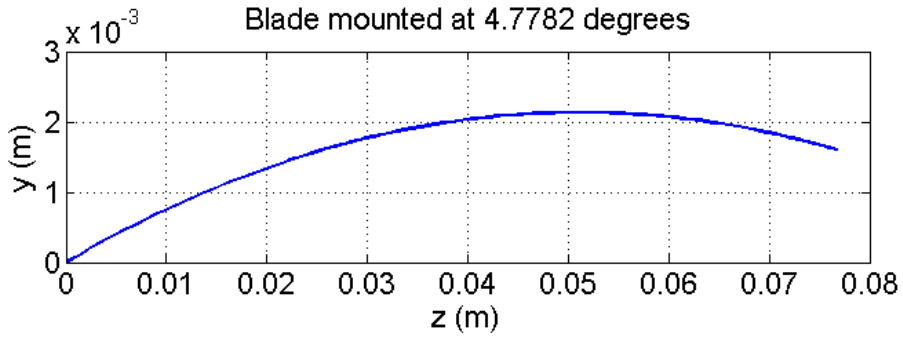

Figure 4 : *Blade profile for small suspension.*

2.4 OSEM diagonalzation

To control the mass under vacuum, we use devices called OSEMs (Optical Sensing Electro-Magnets). These are devices (see fig. 6) that sense the position of an optic using magnets which are mounted on the optic. The magnet partially blocks light from an LED, so when it moves it causes changes in the voltage out from a photodiode. This signal is sent to the digital system, where it is converted into position, pitch, yaw, and side motion. Each of these degrees of freedom have specific filters applied to them, then the signals are converted back into the five sensor distances. Coils in the OSEM are driven accordingy, controlling the motion of the optic.

The hardest part to get right when using OSEMs is to properly diagonalize them so that you can push in the standard degrees of freedom (i.e. position, pitch, yaw, and side). This is accomplished in two steps, along with some sneaky meter-to-radian conversion.

First, we diagonalize the input matrix. An ideal input matrix should look like table 3. The input values are converted to micrometers before they get to this matrix. This matrix then converts the measurements to position and side measurements in

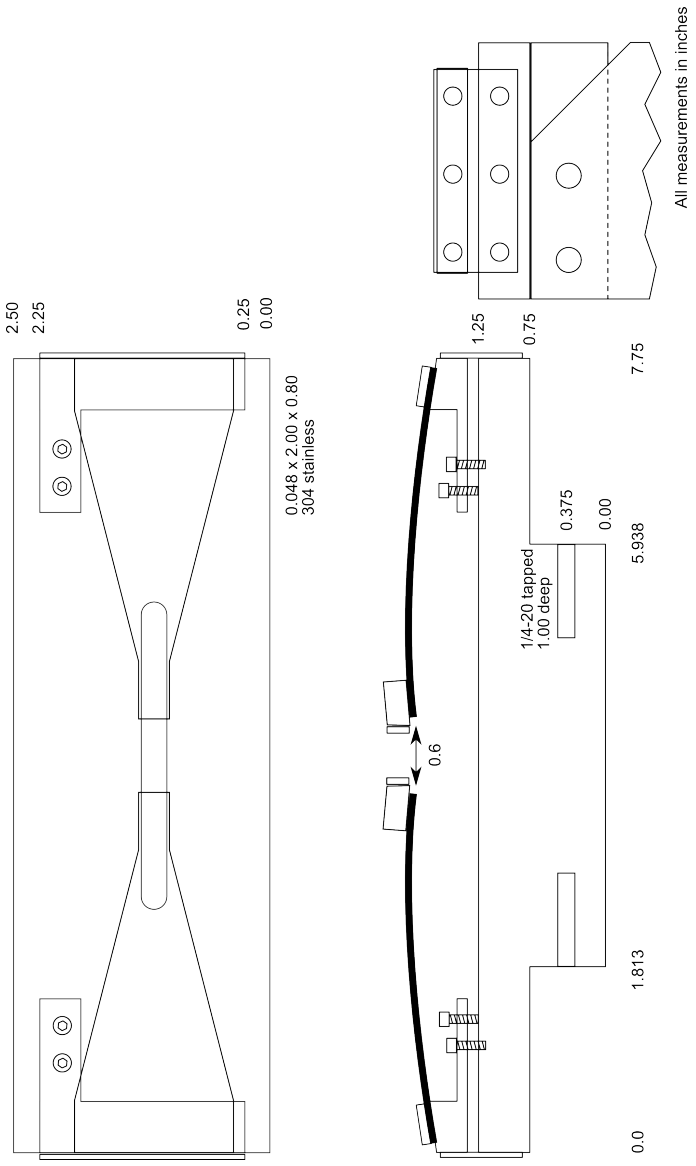

Figure 5 : *Small blade design*

μm and pitch and yaw measurements in μrad (the angular conversion is dependent on the fact that the magnets are mounted in a 4.94 by 4.94 cm square). Thus a change of $1\mu m$ the upper left (UL) sensor is counted as : $.25\mu m$ position, $-10.1\mu rad$ in pitch, $10.1\mu rad$ in yaw, and no change in side.

UL	**UR**	**LR**	**LL**	**SD**	
.25	.25	.25	.25	0	pos
-10.1	-10.1	10.1	10.1	0	pit
10.1	-10.1	-10.1	10.1	0	yaw
0	0	0	0	1	side

Table 3 : Ideal input matrix

However, due to OSEM alignment, machining defects, suspension inaccuracy, etc. the ideal matrix is not the most effective. Thus, we have a method for diagonalizing the matrices.

We drive one OSEM and look at the transfer function between that and all of the other OSEMs. We can determine from this the different modes (pos, pit, and yaw) by looking at the phase differences between the four back OSEMs (UL UR LL LR) at resonances. After this, we orthogonalize based on the coupling of each mode to the five osems. Here we have one interesting note: the position mode that we see is actually the pendulum mode, which is a combination of the pitch and position modes of the mass. The coupling scales inversely with the pendulum length.

Once we have the input matrix set, we diagonalize the output matrix. We close the loops and drive each degree of freedom with a slow signal, then measure the responses in each of the (properly diagonalized) sensors. We subtract out the drive to the not desired degrees of freedom to determine the output matrix.

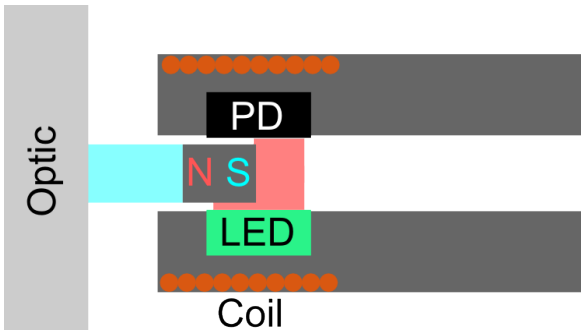

Figure 6 : Layout of an Optical Sensing Electro-Magnet (OSEM). Optic motion is sensed when the magnet changes the amount of light from the light emitting diode (LED) that gets to the photodiode (PD). The coils can be driven to move the magnet and thus the optic.

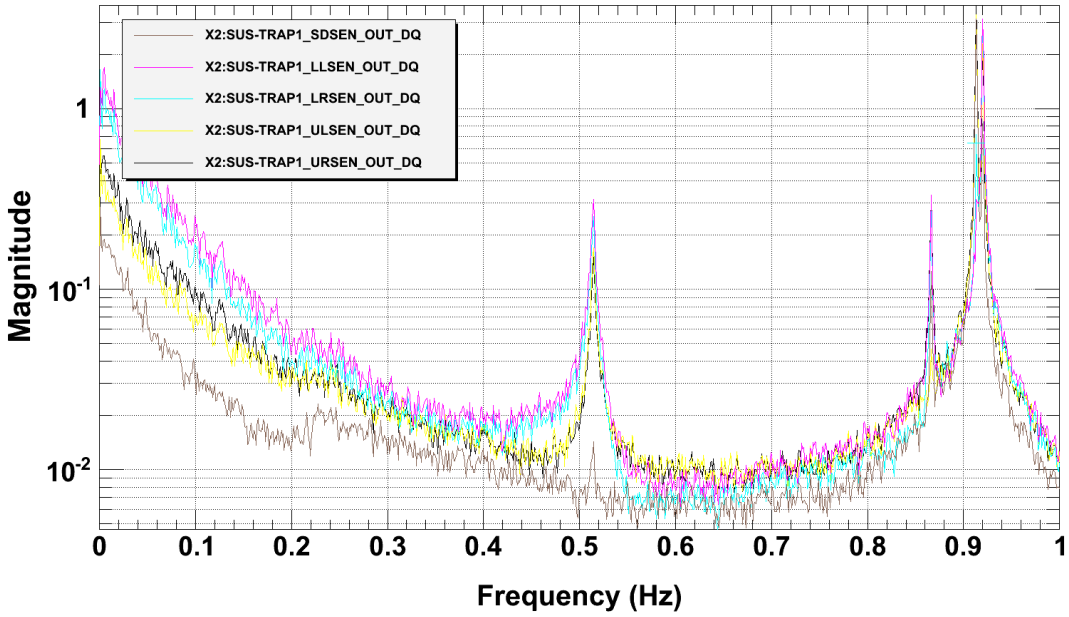

Figure 7 : Spectrum showing the modes of the input coupler. Modes from low to high are: Pitch (0.511 Hz), Yaw (0.866 Hz), Side (0.911 Hz), and Position (0.918 Hz).

Figure 8 : Plot showing the nosie before and after diagonalization

Chapter 3

Control Loops

3.1 Subcarrier Servo

the subcarrier servo is designed to lock a VCO (voltage controlled oscillator) a set frequency away from a crystal oscillator. The is accomplished through two mixers and some feedback.

We typically monitor two spots in this system: The output of the fast mixer (ZMY-3) and the drive signal from the variable oscillator (200 KHz on the diagram). When locked, the two should have the same frequency and be phase locked.

3.2 Method

We are going to look at the spectrum of the oscillators near 80 MHz to figure out the amount of frequency noise from these oscillaotrs. We're mostly concerned with the freqeuncy noise at 1 KHz.

We begin by assuming that all voltage noise is phase noise (no change in the amplitude). This method gives an upper limit to the noise in the system.

ω_m is a measurement frequency. ω_c is the carrier frequency

$$V(t) = V_0 e^{i(\omega_c t + \phi(t))}$$

In the frequency domain,

$$\delta V(\omega_m) = V_0 \delta\phi(\omega_m) = \frac{2\pi V_0}{\omega_m} \delta f(\omega_m)$$

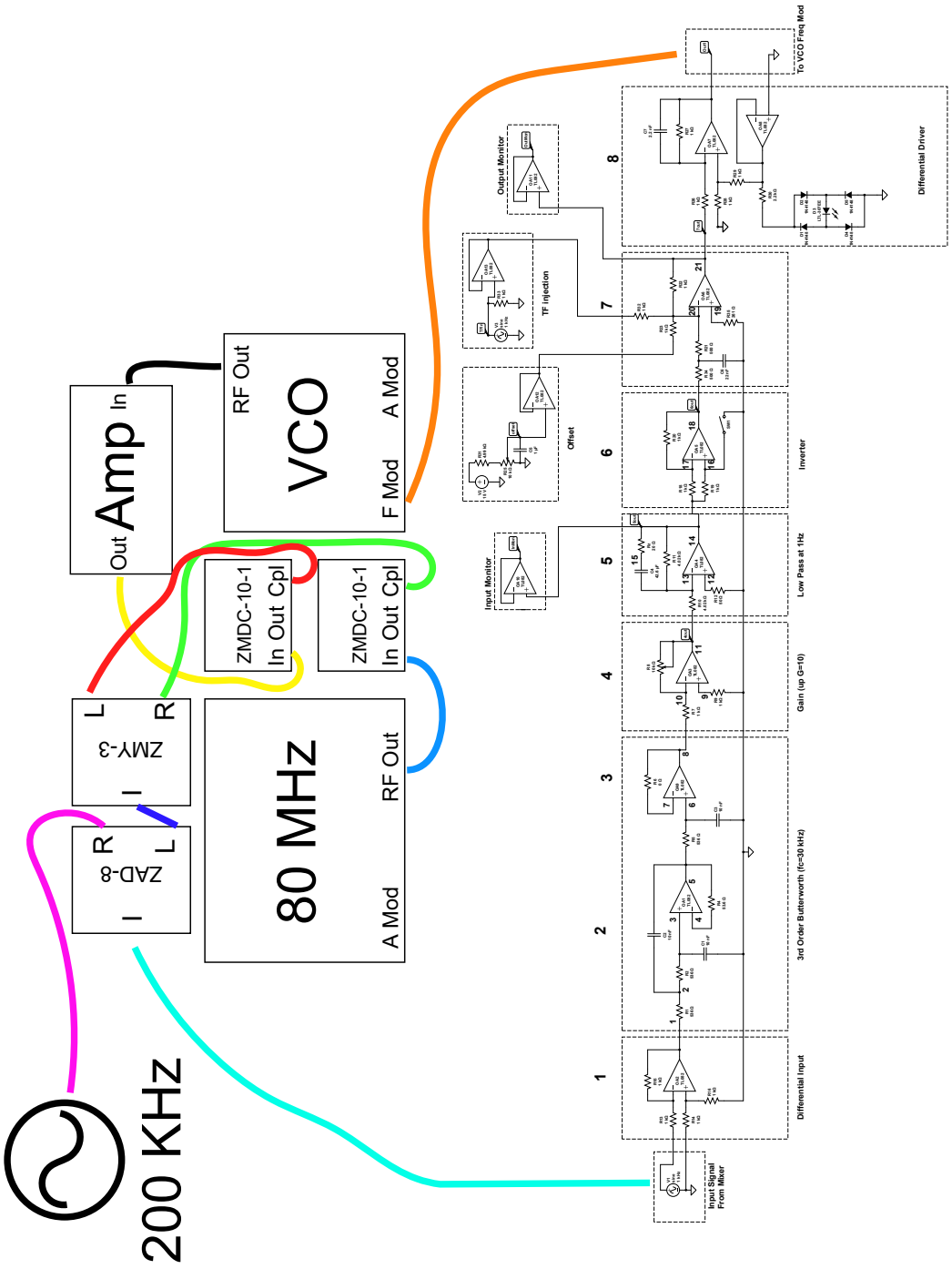

Figure 9 : Subcarrier Servo

Keep in mind that to do this properly, you need to sum the effects of the noise at the carrier plus 1 KHz and the carrier minus 1 KHz.

$$\delta f(\omega_m) = \frac{\omega_m \delta V(\omega_m)}{2\pi V_0}$$

We can now calculate the effect of this frequency noisee on our optical trap cavity. f_L is the laser frequency.

$$\delta x = \frac{L}{f_L}\delta f = 2.66 \times 10^{-16}\delta f$$

The noise budget gives a noise floor of 10^{-17}, so to get in under that, we need a $\delta f << \frac{1}{26.6}$

3.3 Results

With the subcarrier servo locked at approximately 200 KHz, the noises we measure are:

80 MHz Oscillator: frequency noise $5.4 \times 10^{-3}\frac{Hz}{\sqrt{Hz}}$. Position noise $1.4^{-18}\frac{m}{\sqrt{Hz}}$.

VCO: frequency noise $6.7 \times 10^{-2}\frac{Hz}{\sqrt{Hz}}$. Position noise $1.7^{-17}\frac{m}{\sqrt{Hz}}$.

These noise values are OK for the 80 MHz oscillator, but not so much for the VCO. We suspect that the 200 KHz oscillator may be the culprit.

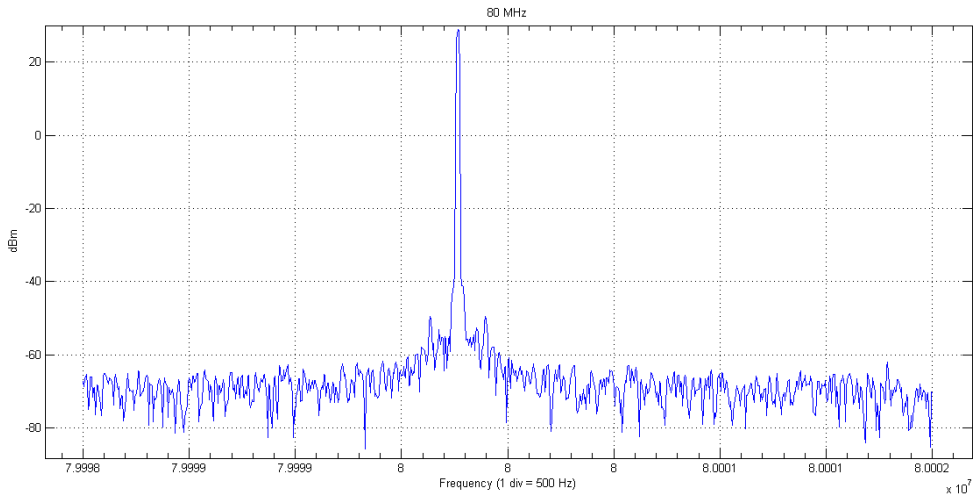

Figure 10 : 80 MHz

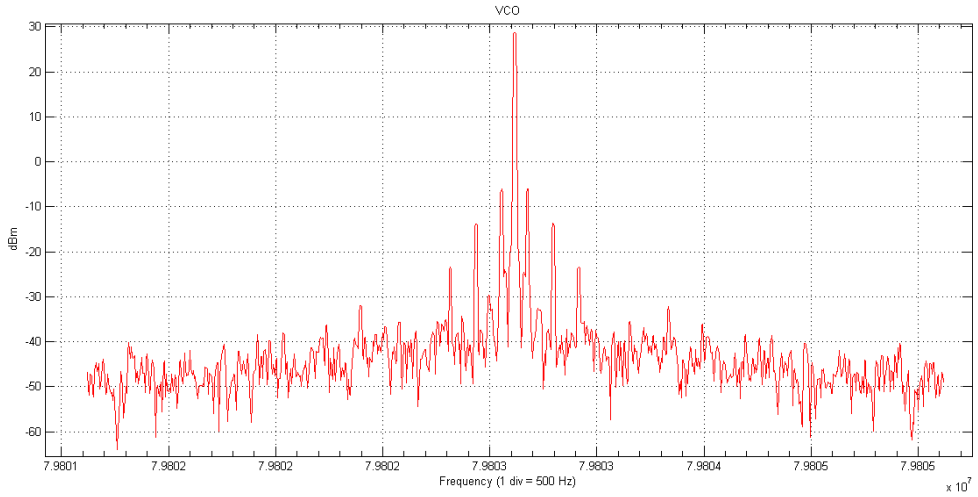

Figure 11 : VCO

3.4 Loops

Here's a picture of the longitudinal trap as it stands. In general terms, we have a cavity with position and laser feedback, which also has optical spring behavior. Analog and digital loops are shown in figures 12 and 13.

You may notice that this layout drawing has an alphabet soup of sections and subsections. I will now describe in excruciating detail what each of these things are and why we care. I am leaving out the input whitening in analog land and the dewhitening in digital land. They should cancel out every time, so we just leave them off. I started drawing in angular control loops, but I won't be addressing them here.

Our goal is to be able to reconstruct the entire optical trap from the control point to the error signal. In our measurements, we are using the injection input and the two test outputs of the Trap Servo board. Test out A serves as our error signal (OUT) and Test out B serves as our control signal (IN). The injection happens between the two test outputs. The resulting open loop transfer function is (plotted in figure 15)

This is based on Jim's model of the loop, which I have updated and repackaged.

$$\left[FHLM + \frac{FAECP + FTCP}{1 + PCED}\right] \frac{1}{1 + SO} \tag{3.1}$$

There are several diffent parts to this equation, so we will take a moment to look each term. Every term in the numerator includes F, the Trap Servo. $FHLM$ is a

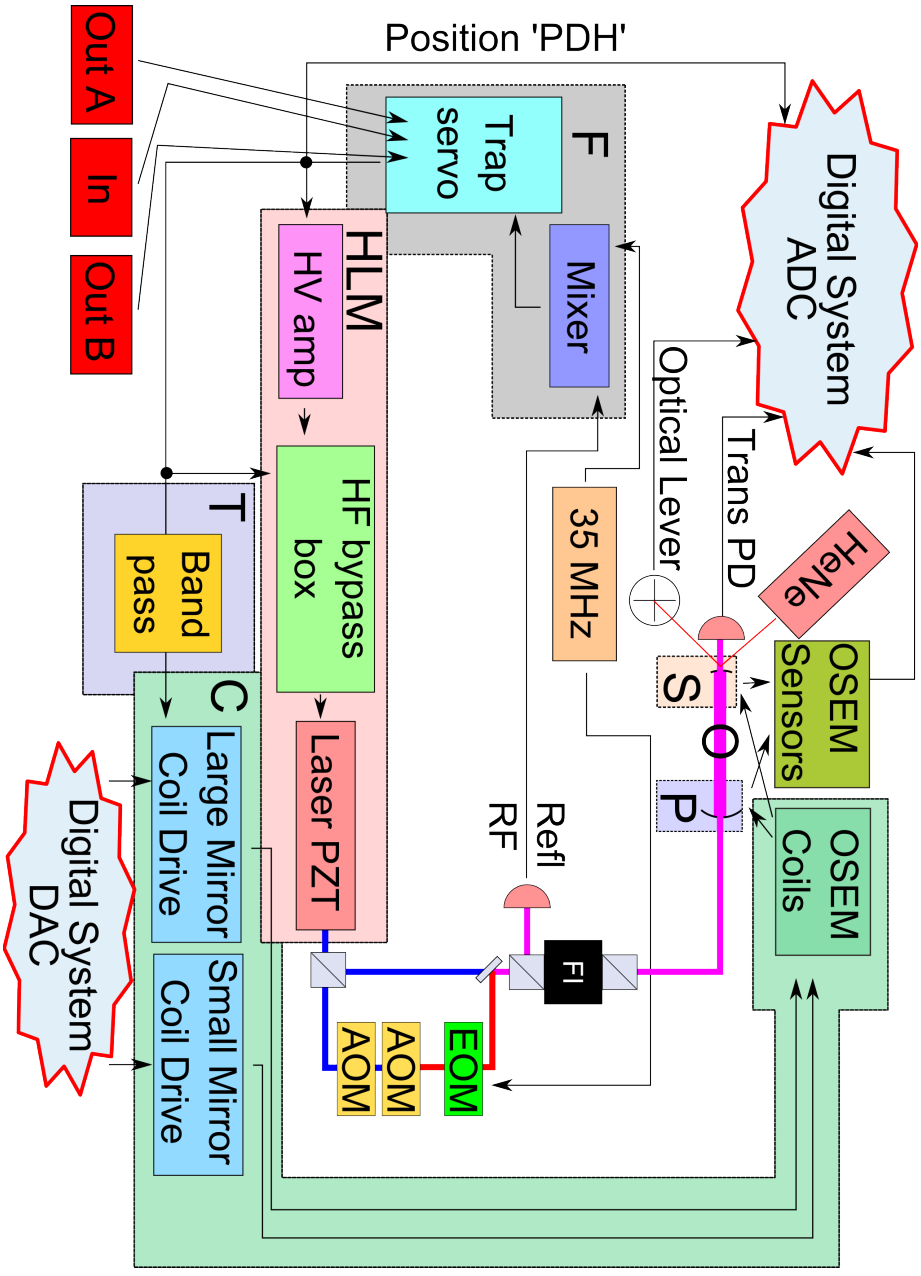

Figure 12 : Analog parts of the locking loop.

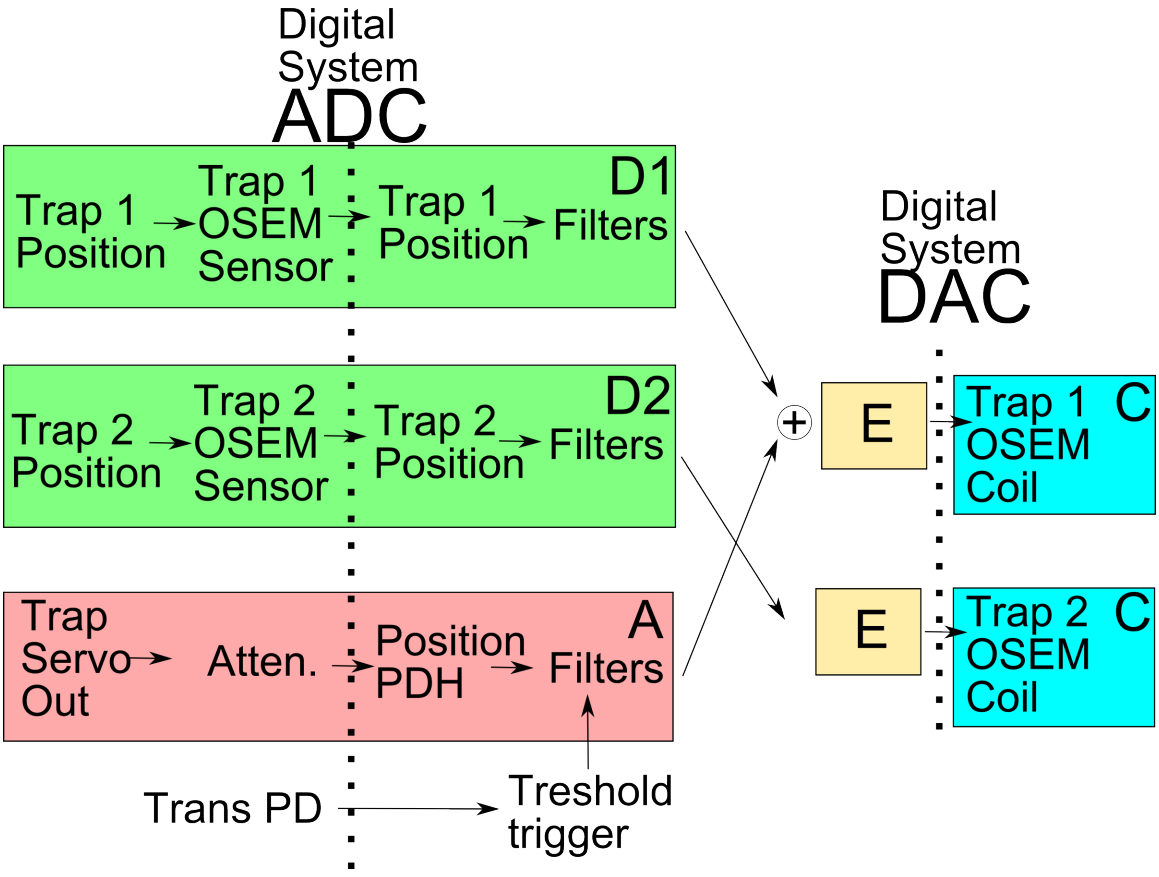

Figure 13 : Digital parts of the locking loop. The yaw and optical lever inputs are not relevant to the longitudinal trap.

loop involving the PZT drive of the laser. $FAECP$ and $FTCP$ both rely on pushing the large mass around using the OSEM drive, but $FAECP$ does the drive through the digital system while $FTCP$ uses an analog connection. $1 + PCED$ is the closed loop of the active suspension damping for the large mass; note that this only affects the loops that are driving the large mass. $1 + SO$ is the closed loop system of the optical spring, which is dependent on the seperation between the two mirrors, rather than the absolute position of either.

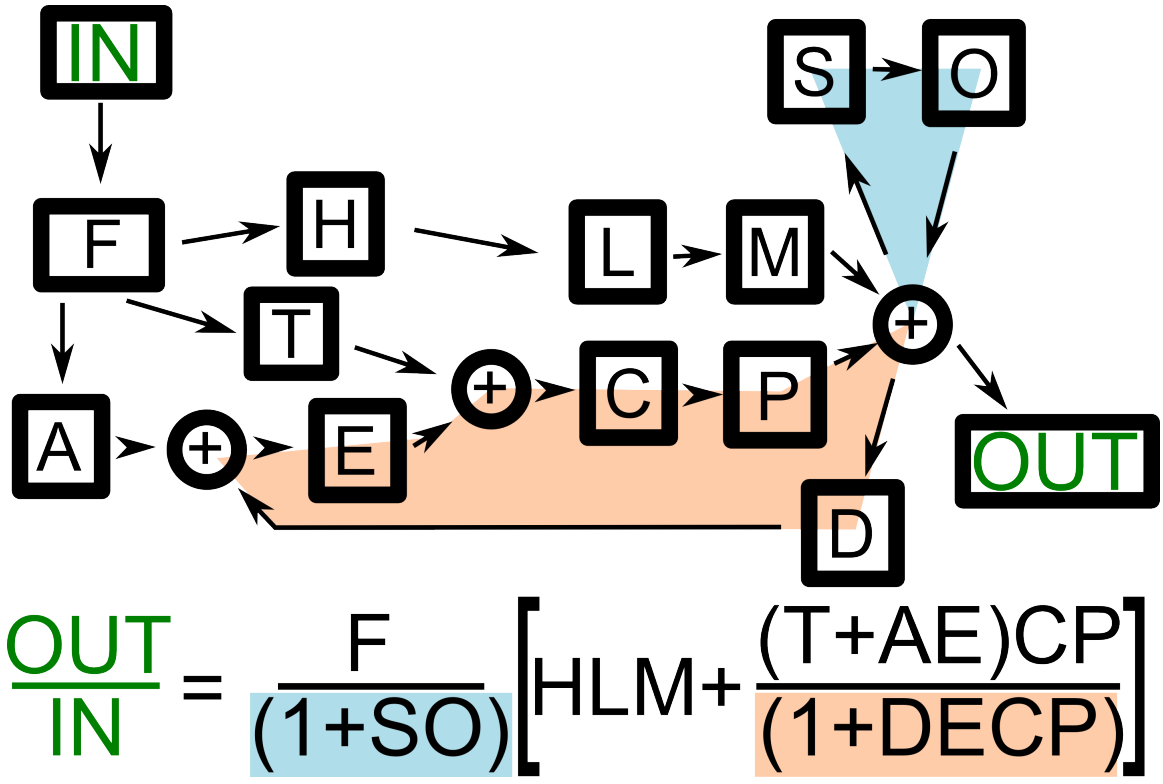

Figure 14 : Block diagram of the open loop TF

3.4.1 A

At the moment, this path has been disconnected, because it was not required. Thus we can set $A = 0$.

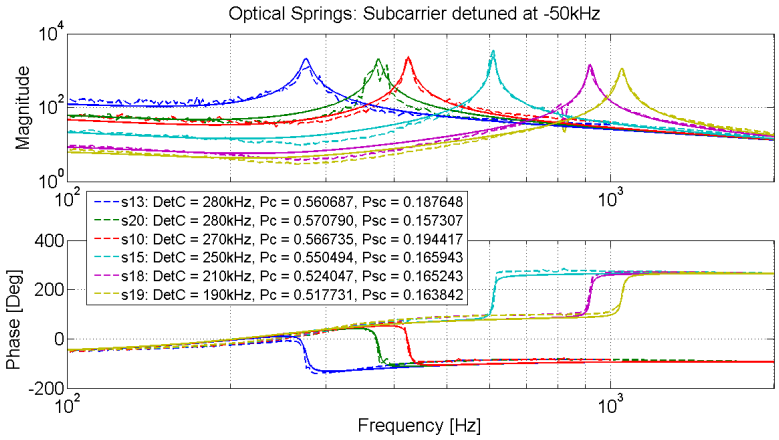

Figure 15 : Open loop TF of several springs, measured vs. modeled.

3.4.2 C

Converts voltage from the DAC into force on the large mirror via the OSEMs. Factor of 4 because we have 4 OSEMs. Number comes from logbook 439.

$$C = \frac{4}{4.91793 \times 10^4 \mathrm{V/N}} \tag{3.2}$$

3.4.3 D1 and D2

The input to each of these blocks the motion of a single optic relative to the OSEMs. The OSEMs put out a current proportional to the position of the mass, which is digitized. The output is a drive signal which gets added into the OSEM drive of trap 1 and trap 2, respectively. The position measurements from each optic have filters applied from the TRAP1_SUSPOS and TRAP2_SUSPOS filter banks. In D1, we have an AC coupling filter(Z: 0, P: 0.5), a highpass (Z: 1, P: 100), and a fourth order Chebychev lowpass filter at 200Hz with 1dB of passband ripple (P: $67.3977 \pm \imath 81.4946$, $27.9074 \pm \imath 196.677$ G: -0.891251). There is also a gain of 10, which includes the filter gain, the conversion of position of the optics relative to the OSEMs into voltage, and the conversion from volts to meters in the digital system. See fig. 16.

From the Matlab code:

```
tf = (1i*freq - 0) .* (1i*freq - 1)...
    ./ (1 + 1i*freq / 0.5)...
```

```
./ (1 + 1i*freq / 100)...
./ (1 + 1i*freq / (67.3977+1i*81.4946))...
./ (1 + 1i*freq / (67.3977-1i*81.4946))...
./ (1 + 1i*freq / (27.9074+1i*196.677))...
./ (1 + 1i*freq / (27.9074-1i*196.677))...
.* -0.891251...
.* Dgain;
```

Why don't we consider the effects of D2? Because we are not putting any active drive through it. Thus it will not shape the loop as drastically as D1. The coupling between the mirror position and the ring position drop off drastically (f^{-2}) above the position resonance of the glass suspension ($\approx$ 18Hz). As we improve the lock, we expect that we will be able to reduce or even remove active feedback on the ring.

3.4.4 E

Converts force output of digital filters into volts so that you can send it out of the digital system. Factor of 4 because we have 4 OSEMs. Note that $CE = 1$.

$$E = \frac{1}{4} 4.91793 \times 10^4 \text{V/N} \tag{3.3}$$

3.4.5 F

This is the transfer function of the Trap Servo, the RF photodiode, and the mixer. Input to this is the cavity length, read out through the PDH method. The output is a voltage. The variable 'mxrpd,' which is the conversion from cavity length to the voltage output of the mixer, is dependent on power, cavity mode matching, and the PDH readout at the mixer. mxrpd, measured at full power, just below the oscillation point, is about 10^9 V/m. See fig. 17. At the moment, we are only using the 100Hz integrator. This has been modeled completely with the 'Analog' library in /software/matlab/analog.

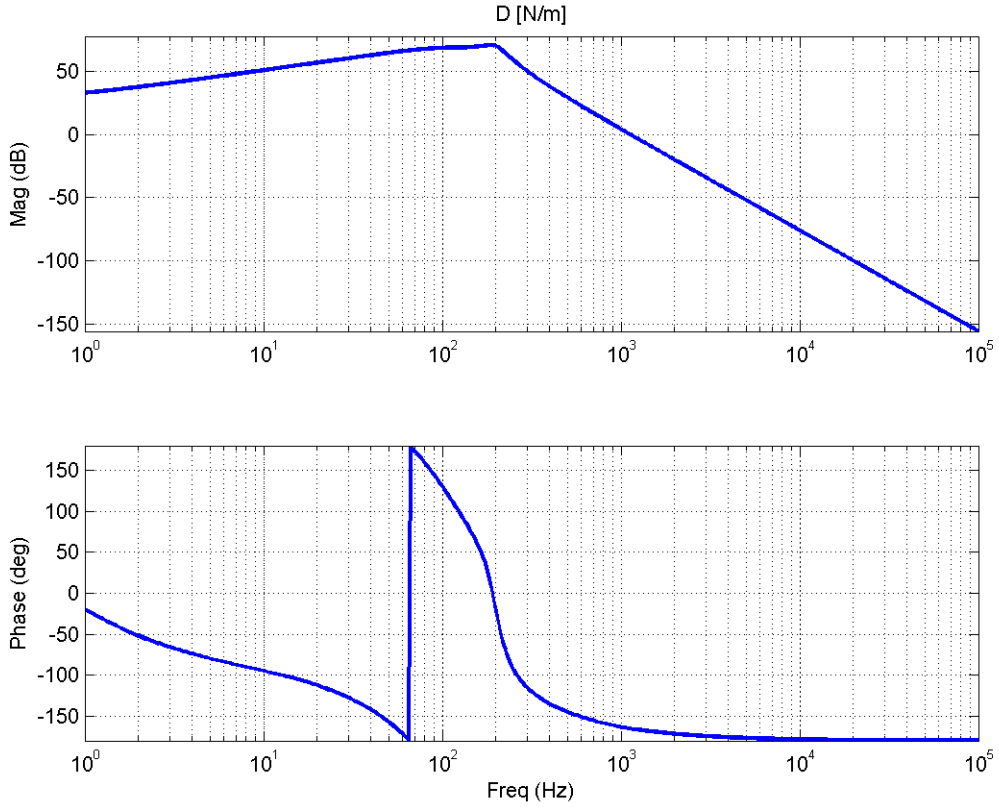

Figure 16 : D1, the transfer function from the position of optic 1, the input coupler, to a digital drive force.

3.4.6 P

Pendulum of the large mass. Converts a force to a displacement in the position direction. Resonant frequency $f_L = 1.4$Hz. Large mass $m_L = 300$g.

$$P = \frac{1}{m_L(2\pi f_L)^2} \frac{1}{\left(1 - \left[\frac{f}{f_L}\right]^2\right)} \tag{3.4}$$

3.4.7 S

The glass suspension connects the small optic to the ring; it acts as a high-Q spring. An optical lever is used to damp oscillation modes other than the position mode.

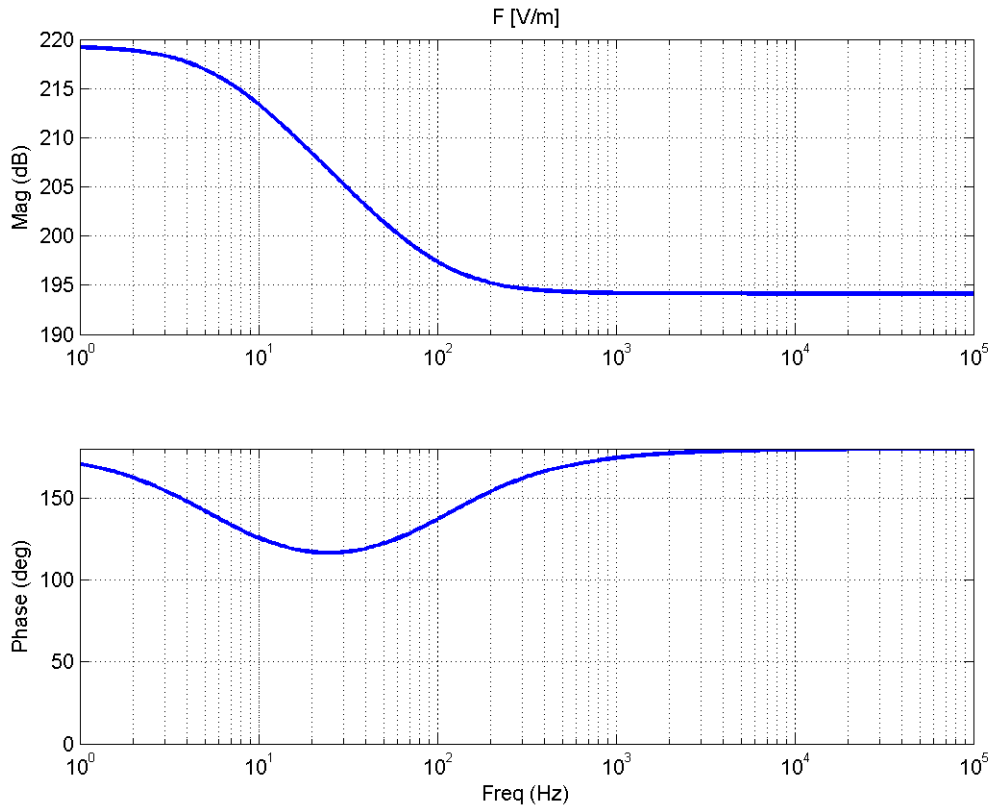

Figure 17 : Calculated trap servo TF

It converts a force to a displacement in the position direction. Resonant frequency $f_s = 18$Hz. Small mass $m_s = 0.5$g.

$$S = \frac{1}{m_s(2\pi f_s)^2} \frac{1}{\left(1 - \left[\frac{f}{f_s}\right]^2\right)} \tag{3.5}$$

3.4.8 O

Optical spring! Depending on detunings and power ratio, we should get stable or unstable behavior. Plotted in figure 19. We should note that optical losses before the cavity have to be considered when determining the power in the cavity, as well as the cavity detuning and angular displacements of the mirrors. At the moment we are calculating this using Finesse.

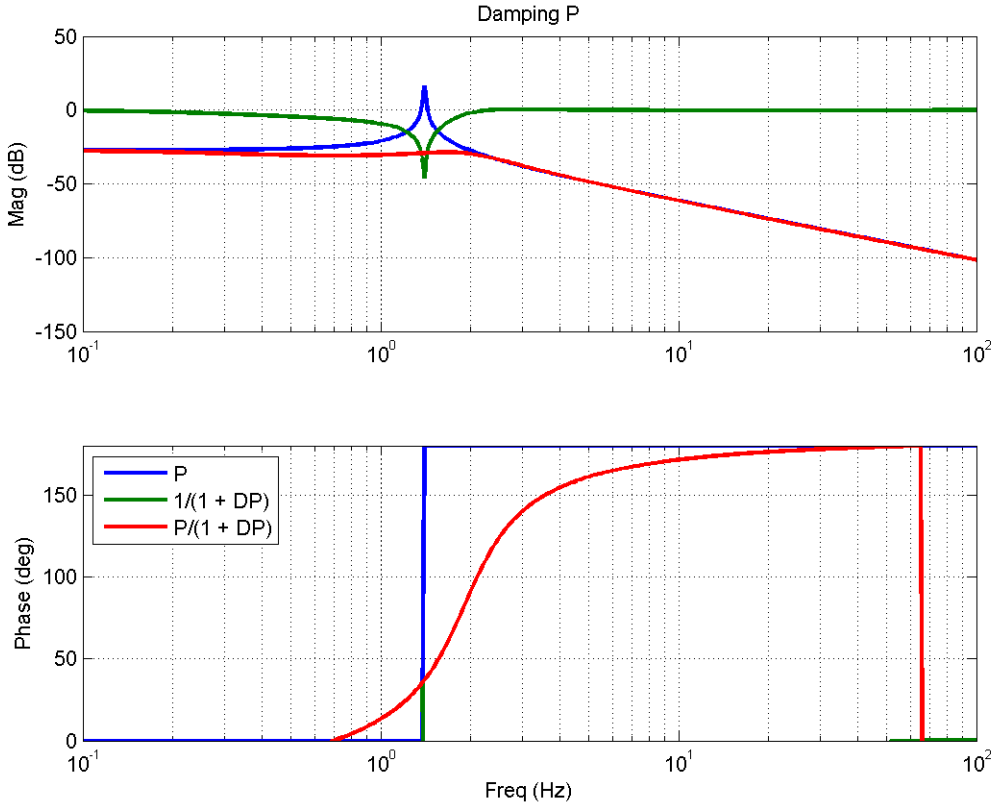

Figure 18 : Damped large mass pendulum

Combining this spring constant with S in a closed loop gives us the behaviour of the optical spring on the small mass, and thus cavity length. Below, in equation 3.6, is the effect of the optical and mechanical springs on changes in the cavity length.

$$\frac{1}{1+OS} = \frac{k_m - m\omega^2}{k_m + k_{os} - m\omega^2} \tag{3.6}$$

3.4.9 L

Laser PZT. Converts a voltage to a shift in the laser frequency. From product spec sheet.

$$L = -1.7 \times 10^6 \text{Hz/V} \tag{3.7}$$

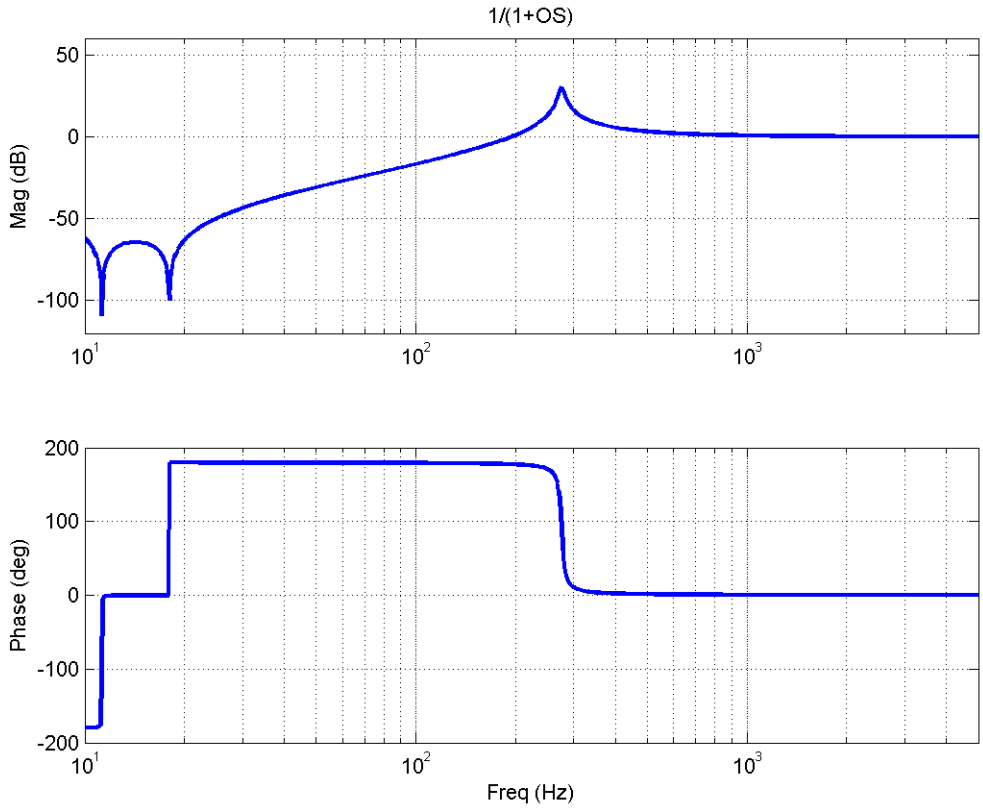

Figure 19 : Plot of the closed loop behavior of the spring doing springy things. The 1 Hz resonance should probably be suppressed by the digital system damping loop

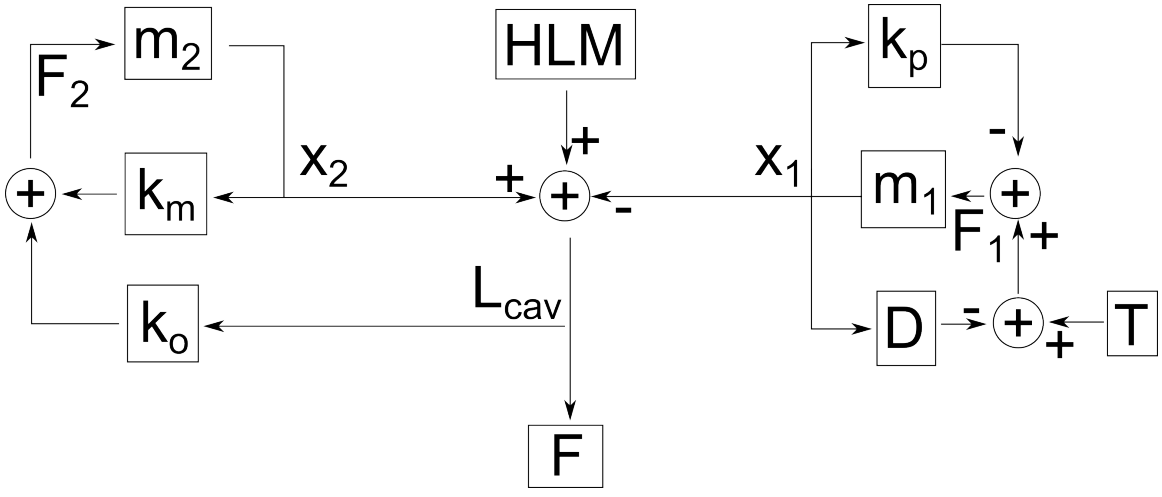

Figure 20 : Those blocks demonstrate WHY we can simply multiply the loop TF by the CLG of the optical spring

3.4.10 M

Cavity. Small change in laser frequency can be converted into a small change in cavity length. Cavity length $l = 0.07$m

$$M = \frac{l\lambda_0}{c} \tag{3.8}$$

3.4.11 H

HV amplifier (with HV bypass) from measurement. See fig. 21. The HV bypass is described in ALog 412. The overall behavior of the amplifier and the bypass is designed to look like this simplified model:

$$H = \frac{70}{1 + \imath f/146} \tag{3.9}$$

We actually interpolate the data for this block, so that we don't run into trouble in the discrepancy region.

3.4.12 T

This is a SR560 that operates between the Trap Servo control signal and the analog drive for the large optic OSEMs.

It is currently set to a 1KHz 6db lowpass with a gain of 200, so it is modeled as

$$T = \frac{200}{1 - \imath f/1\text{KHz}} \tag{3.10}$$

3.5 Photothermal effect on loops

The photothermal effect is directly related to how close the cavity is to resonance. This is affected by the total cavity length and the frequency of the light entering the cavity. In figure 22, we see that the photothermal effect (Pt) can be treated as a closed loop acting on the cavity length L_{cav}.

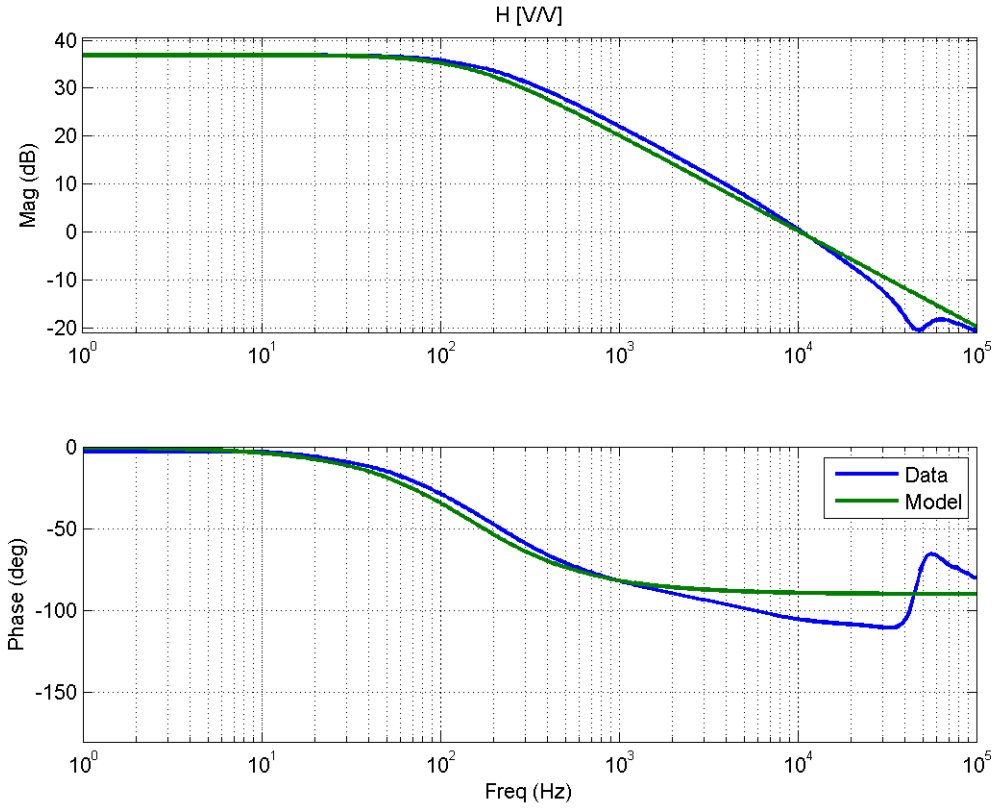

Figure 21 : H transfer function

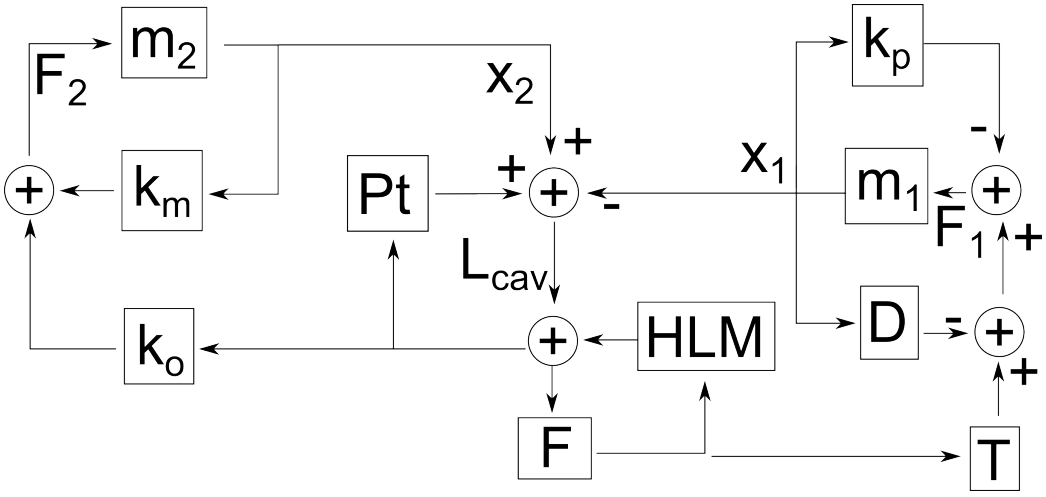

Figure 22 : Loop diagram for a single degree of freedom, including photothermal feedback, Pt.

Chapter 4

Photothermal (from paper)

4.1 Introduction

The Advanced Laser Interferometer Gravitational-Wave Observatory (aLIGO) [3], together with its international partners Virgo [4] and KAGRA [5], aim to directly observe gravitational waves emitted by astrophysical sources such as coalescencing of black hole and neutron star binary systems. The installation of the Advanced LIGO detectors is completed, and commissioning towards the the first observation run is ongoing. Preliminary astrophysical data is expected in 2015. The sensitivity of those advanced gravitational-wave detectors in the observation band is limited by the quantum noise of light and the thermal noise associated with mirror coatings. A contributor to the thermal noise, expected to dominate in future cryogenic gravitational-wave detectors, is thermo-optic noise [6, 7, 1]. It is caused by dissipation through thermal diffusion.

The same physics also leads to an intensity noise coupling, known in the literature as photo-thermal effect [8]. The low frequency behaviour of the photo-thermal effect was predicted in [7] and experimentally measured in a Fabry-Perot cavity by De Rosa et. al. [9]. The physics relevant for the the high frequency behaviour, dominated by the details of the coating, was investigated in [1] in the context of studying thermo-optic noise. It was extended to a full model of the photo-thermal transfer function in [10]. Here we explore the thermo-optic effect in the context of an optical spring. The coupling acts as an additional feed-back path. The phase of the coupling becomes important and can directly affect the stability of the optical spring resonance. We can

exploit this dependence for a precision measurement of the photo-thermal coupling, even if it is driven by the residual few-ppm absorption of a high-quality optic.

The desire to lower the quantum noise in the gravitational-wave observation band has driven the power circulating in the Advanced LIGO arm cavities up to about 800 kW. The high laser power, in turn, couples the angular suspension modes of the two cavity mirrors. This Sidles-Sigg instability [11] creates a soft (unstable) and a hard mode, whose frequency increases with the intra-cavity power. The detector's angular control system must control the soft and damp the hard mode, and at the same time must not contaminate the observation band, starting at 10 Hz in the case of Advanced LIGO. Future gravitational wave detectors aim to extend the observational band to even lower frequencies, further aggravating this limitation. We previously proposed a model [12] to overcome the angular instabilities, based on a dual-carrier optical spring scheme demonstrated by Corbitt et al., in 2007 at the LIGO laboratory [13]. The proposed angular trap setup uses two dual-carrier beams to illuminate two suspended optical cavities which share a single end mirror. As first step towards the experimental demonstration of the scheme we built and operated a prototype, single-cavity optical trap, capable of controlling the cavity length only [14]. The data presented in this paper was taken with this prototype. The next version of the angular trap setup will also allow us to measure the photo-thermal effect on a folding mirror. Heinert et. al. [15] predicted excess thermal noise for folding mirrors due to transverse heat diffusion. The result has not yet been experimentally confirmed, but since the same physics will also lead to an enhanced photo-thermal transfer function, the prediction can be verified with a photo-thermal transfer function measurement.

The paper is structured as follows: Sections 4.2 and 4.3 will review the idea of a dual-carrier optical spring and the photo-thermal effect respectively. Section 4.4 describes the experimental setup and we discuss the result in section 4.5. Finally, section 4.6 suggests a coating modification to make a single-carrier optical spring feasable.

4.2 Dual-carrier optical spring

A Fabry-Perot cavity detuned from resonance couples the intra-cavity power linearly to the mirror position. The response is delayed by the cavity storage time. The

resulting optical spring constant is given by [12].

$$K_{OS}^{\text{1field}} \approx K_0 \frac{1}{1+\frac{\delta^2}{\gamma^2}-\frac{\Omega^2}{\gamma^2}+i2\frac{\Omega}{\gamma}} \tag{4.1}$$

$$K_0 = P_0 t_1^2 r_2^2 \frac{8kr_1r_2}{c(1-r_1r_2)^3} \frac{\frac{\delta}{\gamma}}{(1+\frac{\delta^2}{\gamma^2})} \tag{4.2}$$

where P_0 is the incident power, corrected for mode-matching losses, $k = 2\pi/\lambda$ is the wave vector of the light, t_i and r_i are the mirror amplitude transmissivity and reflectivity for input coupler ($i = 1$) and end mirror ($i = 2$), and γ, δ and Ω are the cavity line, cavity detuning, and mechanical frequency. The value of K_{OS} lies in either the 2nd or 4th quadrant of the complex plane, and the associated radiation pressure force creates either a anti-restoring and damping (red detuning) or a restoring and anti-damping force (blue detuning) [16].

Two spatially overlapping optical fields, the carrier and sub-carrier, with opposite detuning sign and with an opportune power ratio can be used to cancel the instability [13]. The total optical spring K_{OS} is the sum of the individual springs

$$K_{OS} = K_{OS}^{c} + K_{OS}^{sc} \tag{4.3}$$

Where K_{OS}^{c} and K_{OS}^{sc} are given by equation 4.1. The dual-carrier optical spring can be tuned to lie in the 1st quadrant for the frequency band of interest. When acting on a suspended cavity end mirror with mass m and mechanical suspension spring constant K_m the optical spring becomes a feed-back loop with a closed loop response function

$$\frac{x}{F_{ext}} = \frac{1}{-m\Omega^2 + K_m + K_{OS}} \tag{4.4}$$

The tunability of the optical spring K_{OS} in both magnitude and phase allows experimental fine-tuning of the poles of equation 4.4 to lie exactly on the real axis, resulting in an infinite Q of the optical spring (critical stablility). Experimentally this can be done up to a maximum Q, above which the measured transfer function data no longer permits distinguishing between a stable and an unstable spring. The phase of the total spring constant at resonance can then be determined with a precision given by $1/Q$. The suspension mechanical spring constant has to have a positive imaginary part, but it can be designed to be very small. Loss angles of 10^{-5} are easily

achievable, and are further diluted by the magnitude of the ratio of K_{OS}/K_m. The contribution to the phase of the total spring constant from the mechanical suspension is thus expected to be negligible. The imaginary part of the optical spring K_{OS} on the other hand is closely related to its real part through equations 4.3 and 4.1, and is very accurately predicted based on the resonance frequency, carrier to sub-carrier power ratio as well as the detuning of carrier and subcarrier, i.e. only power ratios and frequencies. As a result, any deviation in phase from the expectation of equation 4.1 around the optical spring resonance is easily and repeatably observable with a precision given by the inverse of the experimentally resolvable Q, and an accuracy determined only by frequency and power ratio measurements.

4.3 Photo-thermal effect

Power absorption on the surface of an optic leads to an increase of the surface temperature. The depth of the heated layer is given by the diffusion length $d_{\text{diff}} = \sqrt{\kappa/(\rho C \Omega)}$, where κ, C and ρ are the thermal conductivity, heat capacity and density of the material, and Ω is the observation angular frequency. In the large-spot size limit, i.e. $\mathrm{w} \gg d_{\text{diff}}$, and neglecting coating effects, the displacement of the surface is given by (e.g. [7, 10])

$$\triangle z = \bar{\alpha} \int_0^\infty T dz = \bar{\alpha} \frac{j}{i\Omega\rho C} \tag{4.5}$$

where $\bar{\alpha} = 2(1+\sigma)\alpha$ is the effective expansion coefficient under the mechanical constraint that the heated spot is part of a much larger optic [1, 2]. α and σ are the regular linear expansion coefficient and Poisson ratio. $j = P/(\pi \mathrm{w}^2)$ is the absorbed average surface intensity of the Gaussian beam with beam radius w ($1/e^2$ intensity). This simple picture needs two important refinements. First, for frequencies Ω around and below $\Omega_c = 2\kappa/(\rho C \mathrm{w}^2)$ the transverse heat diffusion leads to a multiplicative correction factor to equation 4.5 derived by Cerdonio et al. [7]:

$$I(\Omega/\Omega_c) = \frac{1}{\pi} \int_0^\infty du \int_{-\infty}^\infty dv \frac{u^2 e^{-u^2/2}}{(u^2+v^2)\left(1 + \frac{(u^2+v^2)}{i\Omega/\Omega_c}\right)} \tag{4.6}$$

As expected, for $\Omega \gg \Omega_c$, the correction factor approches 1. For a fused Silica substrate, SiO_2, and a Gaussian beam spot radius of $\mathrm{w} = 161$ μm this correction

becomes large below $\Omega_c/(2\pi) = 10$ Hz, but is measurably different from unity even at 1 kHz. (See fig 23)

Second, for high frequencies, the diffusion length becomes comparable to the coating thickness. Since the optical field is reflected by a dielectric stack, the effective mirror displacement is given by [1, 10]

$$\triangle z = \sum_i \left[\frac{\partial \phi_c}{\partial \phi_i} (\beta_i + \bar{\alpha}_i n_i) + \bar{\alpha}_i \right] \bar{T}_i d_i \tag{4.7}$$

where $\bar{\alpha}_i$, $\beta_i = dn/dT$ and n_i are the constrained effective expansion coefficient, the temperature dependence of the index of refraction, and the index of refraction itself for layer i. $\frac{\partial \phi_c}{\partial \phi_i}$, the dependence of the coating reflected phase on the round trip optical phase in layer i, is always negative, resulting in a sign change and enhancement of the bracket in equation 4.7 for the first few layers. $\bar{T}_i d_i$ is the temperature profile driven by the absorped intensity j, integrated across layer i. For a $Ta_2O_5 : SiO_2$ coating used in gravitational wave detectors we find a measureable enhancement of the photo-thermal transfer function around 1 kHz [10]. Additionally, depending on the detailed absorption profile, a sign change can occur above about 100 kHz.

For the experiment parameters discussed in this paper, i.e. a Gaussian beam spot radius of w = 161 μm and a mirror coating with about 13 doublet layers both effects are relevant in the 100 Hz to 1 kHz band. Their contributions are plotted in figure 23.

4.4 Experimental setup

4.4.1 Cavity

The optical spring cavity is composed of two suspended mirrors in a vacuum chamber, each with radius of curvature RoC = 5 cm and power transmissivity $T = 4.18 \times 10^{-4}$. The measured finesse is 7500±250 and the cavity length is $L_0 = 7.0 \pm 0.2$ cm. We chose a short cavity to minimize frequency noise coupling. The cavity has a free spectral range (FSR) of about 2.14 GHz and cavity pole $f_{pole} = \gamma/(2\pi) = 143$ kHz. The input mirror mass is 300 g, designed to be heavy to make it insensitive to radiation pressure; it is suspended as a single stage pendulum with mechanical resonances, i.e. position, pitch and yaw, close to 1 Hz. The end mirror has a mass of 0.41 ± 0.01 g and is

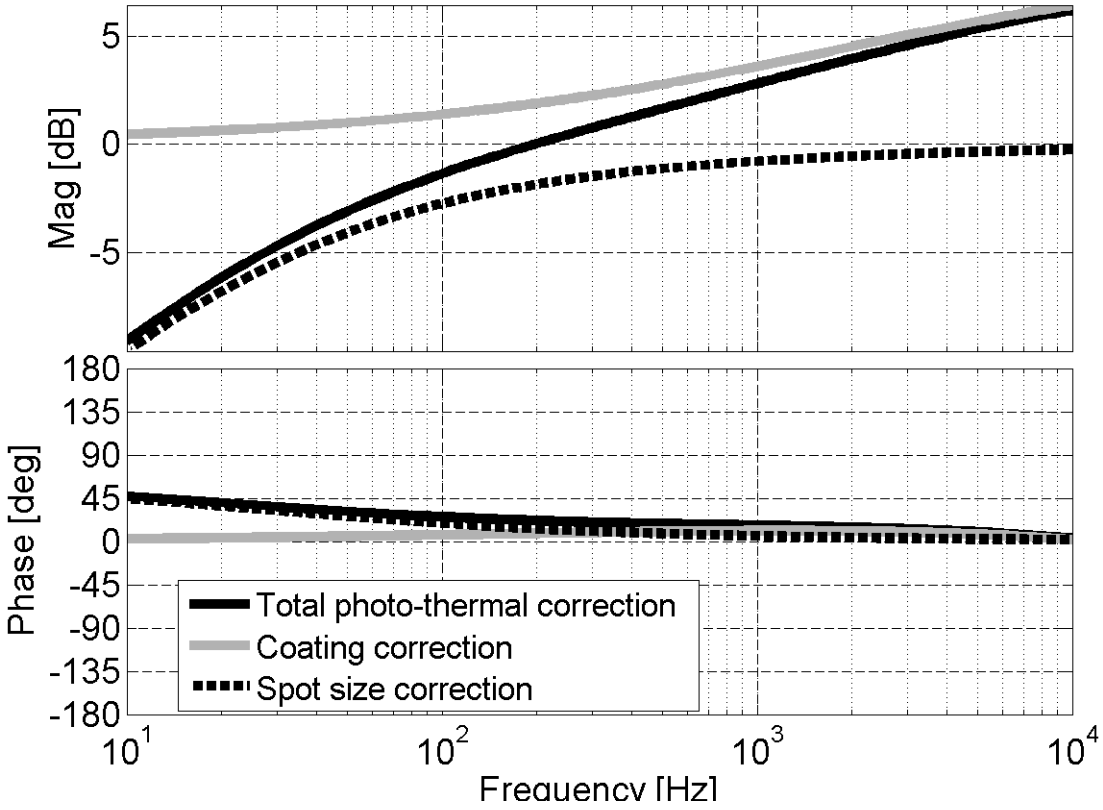

Figure 23 : Correction factors for the photo-thermal transfer function of a fused silica mirror with a dielectric coating (solid black). The solid grey trace is the coating correction for a 13-doublet $\lambda/4$ coating. The dashed black trace shows the effect of a Gaussian beam spot with w = 161 μm radius. To get the full transfer function, multiply with equation 4.5, adding an overall $1/f$ shape. The calculation is based on material parameters show in table 5.

λ_0	1064 nm
Mirror RoC	5.0 cm
L_0	7.0 cm
Spot size	161 μm
FSR	2.14 GHz
Finesse	7500
Cavity Pole	143 KHz

δf_C	213-290 KHz
δf_{SC}	27-36 KHz
P_C input	225-239 mW
P_{SC} input	65-78 mW

Table 4 : Parameters of the optical spring cavity. The range of values for the carrier and sub-carrier detuning frequency (δf_C, δf_{SC}) and input power (P_C, P_{SC}) indicate the variation between individual measurements.

7.75 mm in diameter. It is suspended with three glass fibers from a 300 g steel ring, shown in figure 24. The steel ring has diameter of 7.6 cm and is itself suspended. The input mirror is actively controlled by an electronic feedback system, while the end mirror is free to move in the glass suspension abobe its resonance frequency of 18 Hz, and is only subject to the optical spring radiation pressure.

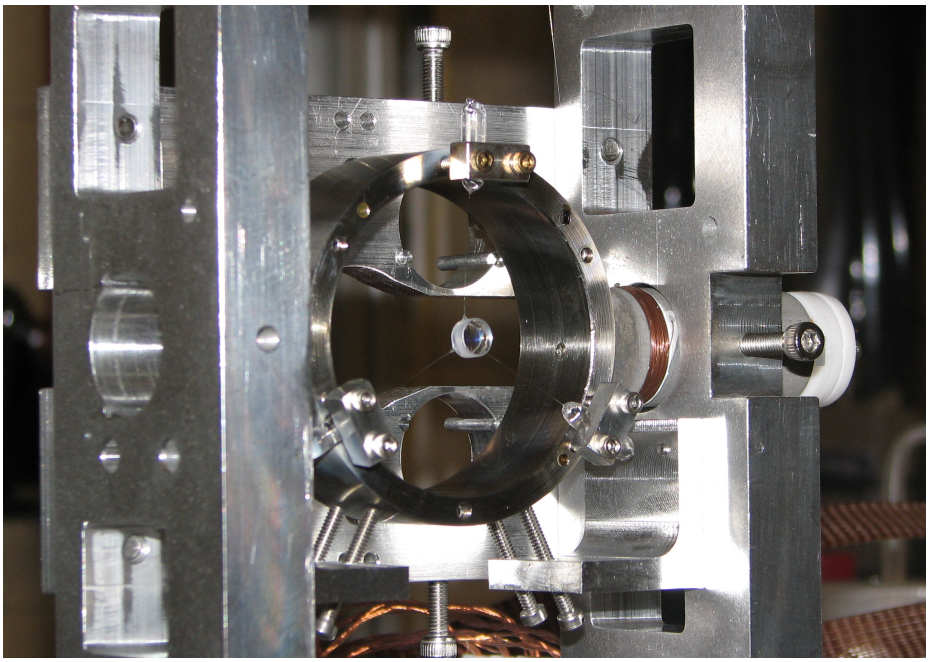

Figure 24 : A picture of the small end mirror suspended from a steel ring by glass fibers. The ring is suspended from a small optics suspension (SOS) with tungsten wire. The SOS provides DC alignment control while allowing the mirror to move freely above the 18Hz resonance of the fiber suspension. The end of the fiber is a small glass nub attached to the mirror with epoxy. This produces a fairly high suspension Q of about $5 \cdot 10^5$. The resulting contribution of damping in the opto-mechanical spring is insignificant compared to the damping from the optical field.

4.4.2 Input field preparation

The optical field incident on the optical spring cavity consists of two beams, a carrier and a subcarrier, as described in Section 4.2. As shown in figure 25, a 1064 nm laser is split into a carrier and a subcarrier beam at the polarizing beam splitter PBS1. In the subcarrier path two acoustic optic modulators (AOMs) are used to impose a relative frequency shift Δ, on the subcarrier beam, leaving it at a set detuning from the carrier beam. Δ is set using an external signal generator (see Sec. 4.4.3). The two

beams recombine at PBS2 and proceed towards the Fabry-Perot cavity with opposite polarization. The total power and the power ratio between the carrier and subcarrier beams are set by two half wave-plates $\lambda/2$.

The subcarrier beam is modulated by a 35 MHz electro-optic modulator (EOM). We measure the modulated light reflected by the cavity with a resonant radio-frequency photodiode (RFPD) and then demodulate to read out the cavity length with the Pound-Drever-Hall technique (PDH) [17]. We use the subcarrier to derive a PDH singal because the subcarrier requires less detuning than the carrier. We can use the PDH signal to actuate on the laser and the suspensions to lock the cavity, then turn down the gain and use the PDH signal for readout.

A small offset added to the PDH error signal shifts the locking point of the cavity to the side of the resonance, setting the subcarrier detuning δ_{sc}. We choose to introduce an offset that corresponds to a negative frequency ("red") detuning. Consequently the carrier is positively ("blue") detuned at $\delta_c = \Delta + \delta_{sc}$. An electronic locking servo can be used to process the error signal and feed back to coils, actuating on magnets mounted on the large cavity mirror, and to the laser frequency.

4.4.3 Subcarrier Servo

The high FSR of our cavity (2.14 GHz) meant that available AOMs, with much lower operating frequency ranges (65 to 95 MHz), were not suitable to lock the carrier and subcarrier on adjacent resonances. However, this same operating range prevents a single AOM from locking the two beams on the same resonance, due to the small cavity linewidth. Thus, we set the subcarrier on the same resonance fringe as the carrier using two AOMs, each one shifting the laser frequency by about 80MHz in opposite directions. One is driven by an 80 MHz crystal oscillator, while the other is driven by a servo-locked Voltage controlled oscillator (VCO) running slightly offset from 80 MHz (see figure 25). To control the offset frequency the 80 MHz signal from the crystal oscillator is mixed with the VCO output, producing a signal at the frequency difference. This difference signal is then mixed with the drive from a function generator, creating the error signal for the servo. The servo drives the frequency modulation input of the VCO, closing the loop and locking the subcarrier beam to a fixed frequency offset from the carrier beam.

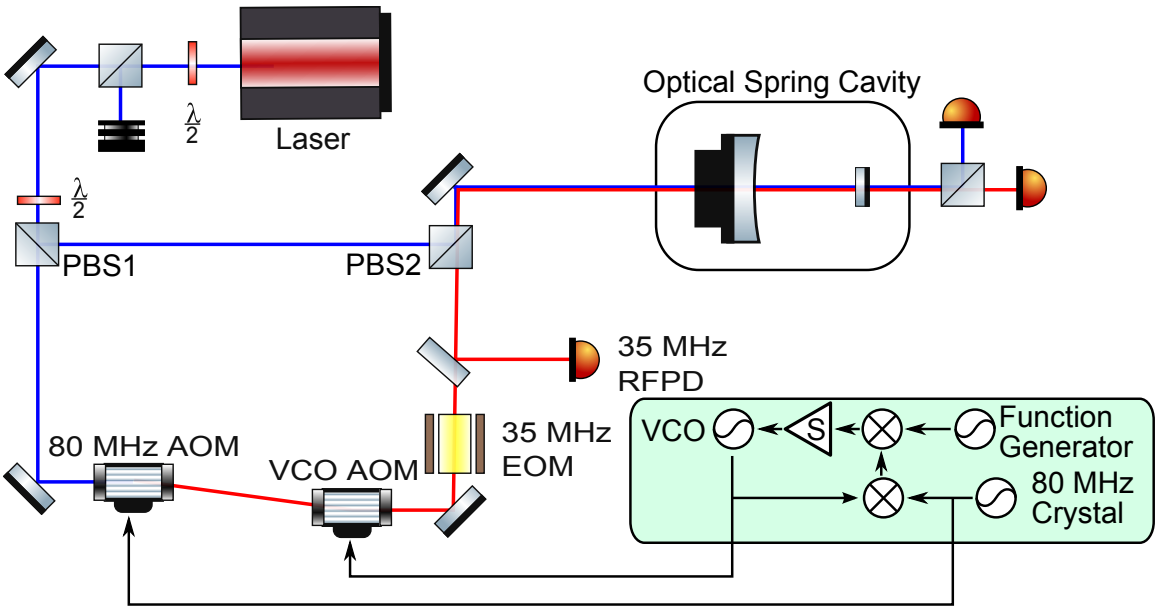

Figure 25 : A schematic layout of the optical trap experiment. The light from the laser is split into the carrier and subcarrier paths at PBS1, with a ratio determined by the $\lambda/2$ plate. The subcarrier path is frequency shifted by two AOMs under the control of the subcarrier servo (described in detail in Section 4.4.3), then recombined with the carrier at PBS2. The co-aligned mode-matched beams enter the cavity, then are individually monitored at the output. We can use the 35 MHz EOM and RFPD in a PDH scheme to read out the cavity length or lock the cavity.

This setup significantly suppresses the frequency noise from the VCO. The remaining subcarrier frequency noise (relative to the carrier) is dominated by fluctuations in the path length difference between carrier and sub-carrier, see figure 25.

4.5 Results

Using the setup described in the previous section, we locked the cavity using a PDH error signal from the sub-carrier, feeding back to the laser frequency actuator and, at low frequencies, the heavy input coupler position. In this configuration we fine-tuned the optical spring parameters (carrier and sub-carrier offset and power) and measured the PDH control loop open loop transfer function. Dividing out the known PDH loop sensing and actuation function gives us the closed loop transfer functions of the optical springs (figure 26). While we demonstrated stable and unstable dual-carrier optical springs, these measurements revealed a significantly smaller phase margin of the optical spring than expected based on equation 4.4, suggesting the presence of a

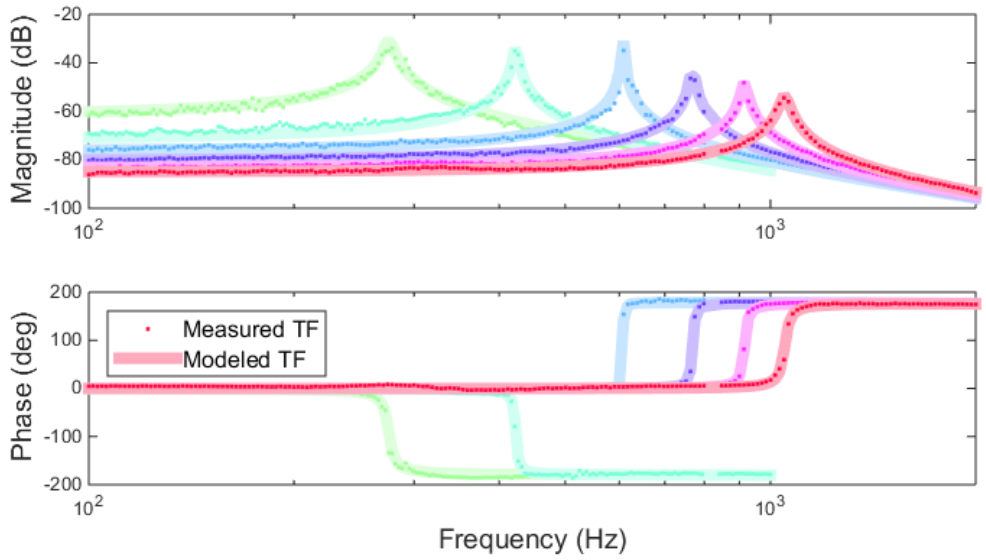

Figure 26 : Data and modeled transfer function for a series of stable and unstable springs. The modeled transfer functions include the full coating and spot size correction, computed with the measured average absorption. Stable springs show a phase drop of 180 degrees at resonance, while unstable springs show a rise of 180 degrees.

non-radiation-pressure feed-back path.

At a few ppm, the absorption A of the mirrors has a very small effect on the cavity finesse and no significant impact on the total transmitted power. However, this small amount of absorption still causes local heating of the optic, driving fluctuations in the surface position of the optic, and thus the cavity length, via the photo-thermal effect. If this is the dominant effect, we should be able to include the photo-thermal effect in our model and fit the model to the data, using the absorption as the free parameter. Given a set of optical spring measurements done under similar conditions, we would then expect to find a consistent absorption coefficient across measurements.

4.5.1 Analysis

For each measured optical spring transfer function we record the carrier and subcarrier transmitted powers, P_{tc} and P_{ts}, the optical spring resonance frequency f_{res}, and the difference between the carrier and subcarrier detunings $df_c - df_s$, which is set by the function generator frequency.

We can then fit the data d using a model m, which includes the photo-thermal

effect. In particular we fit the ratio d/m using a least-squares fit to minimize E, the error.

$$E = \Sigma \left| \frac{d}{m} - 1 \right|^2 \tag{4.8}$$

We fit for a small magnitude offset, the subcarrier detuning df_s, and the absorption A. We assess the fitting errors by modeling the noise in each frequency bin of the transfer function measurement, and propagating this noise through the fit. Four of the optical spring transfer functions had a measurement noise of a little less than 1 dB, while the optical springs at 276 Hz and 422 Hz had a significantly higher noise of about 3 dB. We think this noise is dominated by intra-cavity power fluctuations, most likely due to angular fluctuations.

The remaining parameters (cavity transmitted powers and carrier-sub-carrier frequency spacing) we treat as systematic errors. We propagated their measurment errors through the fit. We used a 2% measurement error for the power measurements and a 1 kHz error for the frequency separation.

After determining the absorption A for each optical spring transfer function measurement, we can take a statistical-error-weighted average to arrive at the most probable absorption coefficient for the mirror. For the full photo-thermal model we measure a consistent absorption of 2.60 ± 0.08 ppm (± 0.06 ppm statistical, ± 0.05 ppm systematic) (see figure 27). The naive $1/f$ model yields an absorption of 3.27 ± 0.10 ppm (± 0.08 ppm statistical, ± 0.06 ppm systematic). The detailed model with coating and spot size corrections is slightly preferred by the data over the naive $1/f$ model, i.e. the result is more consistent with the same absorption at all frequencies. However the errors in our mesurement are too large to make this statement with any sigificant certainty.

Since this measurement is based on the missing optical spring phase on resonance, we can also express the result as extra phase. Near the resonance the optical spring constant is close to real, while the photo-thermal effect is almost purely imaginary. Thus we approximately find for the extra phase ϕ

$$\phi = 2m\Omega^2 \frac{c}{2} \frac{\bar{\alpha}}{\Omega \rho C \mathrm{w}^2 \pi} A I_{\mathrm{corr}} \approx 0.4^\circ \frac{A I_{\mathrm{corr}}}{1 \text{ ppm}} \frac{f}{1 \text{ kHz}} \tag{4.9}$$

Here the leading factor of two accounts for the two mirrors, I_{corr} is the real part of the total correction factor plotted in figure 23, and we used the material parameters

for fused silica (see table 5). Figure 28 shows the measured extra phase on resonance, together with the prediction from the photo-thermal feed-back with the best-fit absorption. The figure also shows the expected phase due to the dual-carrier optical spring, as well as the total phase of the complete model. Finally it is worth mentioning that this is a remarkably precise way to measure the phase of the open loop transfer function - the error bars in figure 28 are as small as 0.04°.

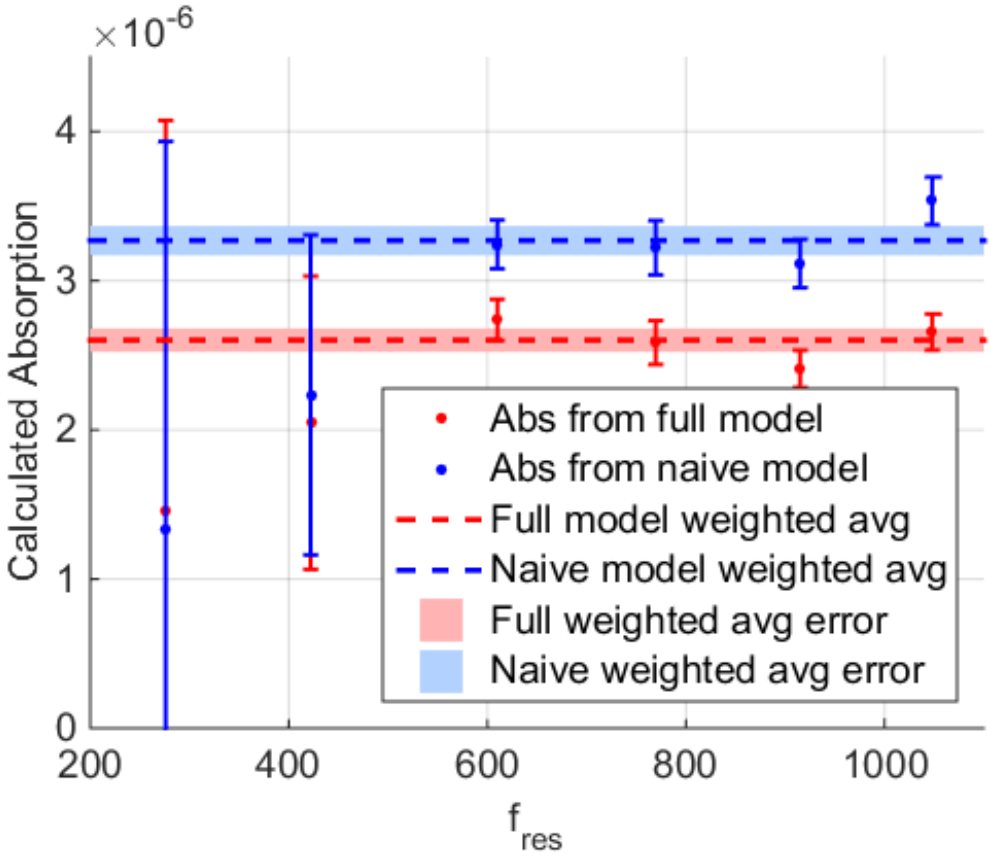

Figure 27 : Absorption fit for naive and full models. The full model absorption is consistent with a constant absorption of 2.60 ± 0.08 ppm. The naive $1/f$ model predicts 3.27 ± 0.10 ppm. The transfer function data for the lowest two resonant frequencies was significantly noisier. Also, at lower frequencies the photo-thermal effect has a smaller effect on the total optical spring. Both effects result in the larger error bars at low frequencies.

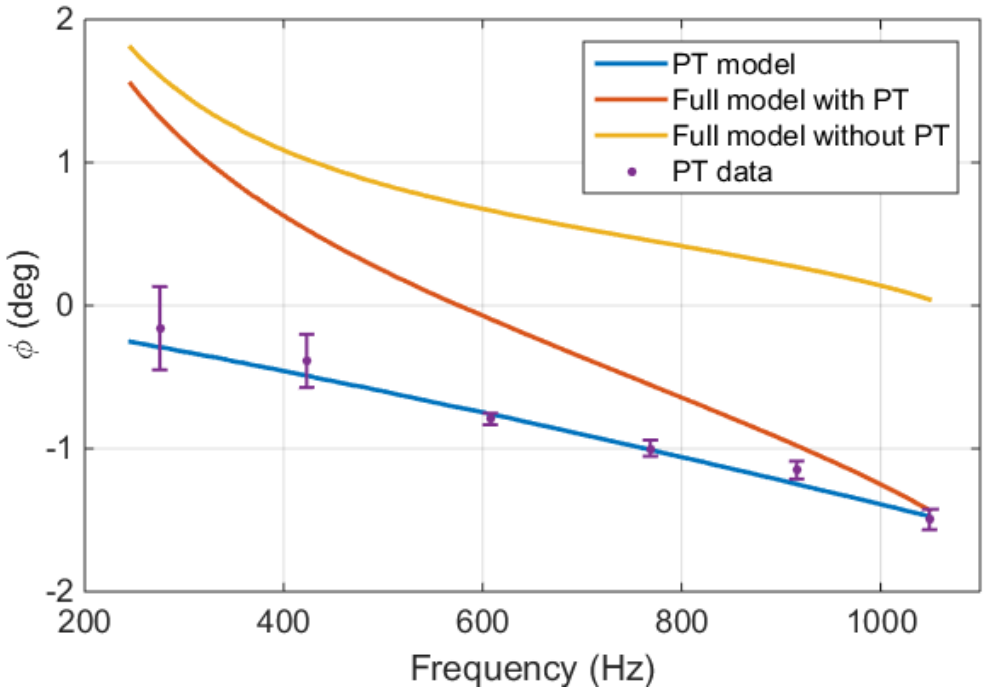

Figure 28 : Feedback phase in the system due to the optical spring and photo-thermal effect. The measured extra phase is consistent with 2.60 ppm of absorption. The error bars are as small as $\pm 0.04°$, a remarkable precision for an open loop transfer function phase measurement.

4.6 Stable single-carrier optical spring

In the experiment at hand the photo-thermal feed-back always pushed the optical spring resonance closer to instability. Perhaps the most interesting question is whether we can change the sign of this feed-back path and exploit it to stabilize an otherwise unstable optical spring. It was pointed out in [10] that this naturally occurs above about 100 kHz for a regular dielectric coating. At those frequencies the thermal diffusion length only affects the first few layers of the coating, which affect the overall coating reflected phase differently than the rest of the coating. However it is actually quite simple to get this sign inversion to occur at a much lower frequency. Increasing the thickness of the inital half-wavelength SiO_2 layer - but keeping it an odd multiple of half the wavelength - will boost the effect from the first layer, thus lowering the frequency at which this sign inversion occurs. Indeed this effect can be strong enough that the damping effect from the sub-carrier is not needed to generate a stable optical spring. To illustrate this, figure 29 shows a set of six optical springs with parameters

identical to the ones shown in figure 26, except that we set the sub-carrier power to zero (i.e. they are single-carrier optical springs), and we increased the first SiO_2 coating layer from 0.5 wavelength to 20.5 wavelength.

Such a modified coating would thus allow detuned self-locking of an optical cavity, using just one laser frequency. It does rely on a small amount (order 1 ppm) of optical absorption in the coating, but this level of absorption is often unavoidable anyway, and does not prevent high-finesse cavities.

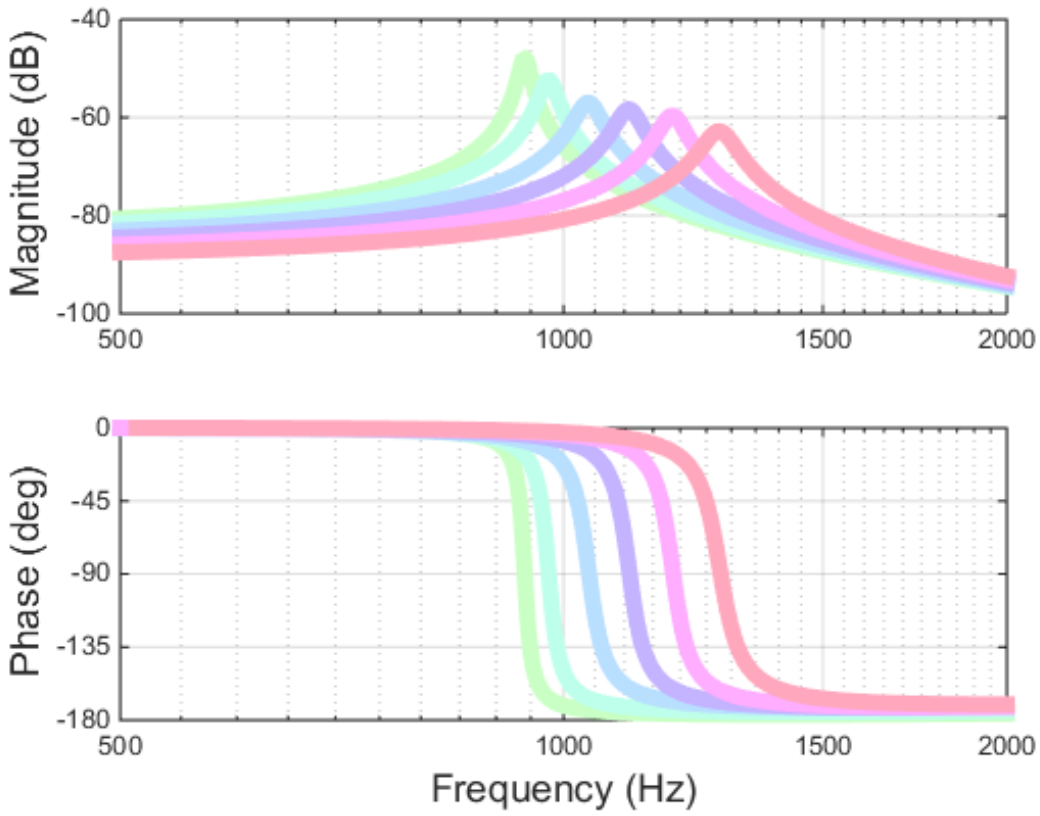

Figure 29 : Stable single-carrier optical springs (no sub-carrier) with modified coating - the first coating layer is 20.5 wavelength thick. See text for details. The six traces otherwise have the same parameters as the best-fit optical springs in figure 26.

4.7 Conclusions

We observed photo-thermal feedback in an experimental optical spring setup for a 0.4 gram mirror. We made measurements for a range of optical spring resonant

frequencies, and used a least squares fit to calculate the absorption. The data is consistent with the predictions of the complete model presented in Section 4.3, but only sligthly prefers it over a simple model that ignores any heat diffusion in the coating and transverse to the optical axis. We also show that a small modification of the first layer of the high-reflectivity coating would be enough to reverse the sign of the photo-thermal feed-back, to the extent that a single-carrier, dynamically and statically stable optical spring becomes feasable.

Repeating the presented measurement with a folding mirror in a cavity should also allow us to confirm the predicted enhancement of thermal noise for folding mirrors [15] . This noise will affect any gravitational-wave interferometer design making use of folding mirrors in the arm cavities [18].

Parameters Ta_2O_5:SiO_2	Symbol	SiO_2	Ta_2O_5	Unit
Refractive Index (@1064 nm)	n	1.45	2.06	-
Specific Heat	C	746	306	J/kg/K
Density	ρ	2200	6850	kg/m^3
Thermal Conductivity	κ	1.38	33	W/m/K
Thermal expansion coef.	α	0.51	3.6	ppm/K
Thermo-Optic coef. (1μm)	$\beta = \frac{dn}{dT}$	8	14	ppm/K
Poisson ratio	σ	0.17	0.23	-
Youngs Modulus	E	72.80	140	GPa

Table 5 : Parameters for fused silica (SiO_2) and tantulum-pentoxide (Ta_2O_5). The values are taken from [1] and [2].

Chapter 5

Angular

5.1 Introduction

The Laser Interferometer Gravitational-wave Observatory (LIGO) is part of a worldwide effort to detect gravitational waves and use them to study the universe [19]. Construction of LIGO's advanced detectors has finished and the first science runs will begin soon. The goal of Advanced LIGO (aLIGO) is the first direct detection of gravitational-waves from astrophysical sources such as coalescing compact binaries and core-collapse supernovae. These detections will open a new spectrum for observing the universe and establish the field of gravitational-wave astronomy. These initial observations will also show the potential science gain of further increasing the state-of-the-art sensitivity of gravitational wave detectors [20, 21, 22]. Such detectors operate near the Standard Quantum Limit, meaning that the contributions from quantum radiation pressure and shot noise are about equal in the observation band [23, 24].

To design a successor to aLIGO, techniques to operate gravitational-wave interferometers below the Standard Quantum Limit need to be developed [25, 26]. Dual carrier control systems and angular control using stable optical springs are promising methods for evading quantum-mechanical limitations on detector sensitivity [27, 28, 29, 30, 31, 16]. In 2007 Corbitt et al. at the LIGO Laboratory at the Massachusetts Institute of Technology demonstrated a one-dimensional optical trap of a one gram mirror using a novel two-carrier scheme [13]. Their work clearly demonstrated the potential of this technique. Extended to angular degrees of freedom, it has

the prospect of opening a completely new approach to the angular control problem in future generation gravitational-wave detectors [32]. Sidles and Sigg have shown that, for a Fabry-Perot cavity with a single resonating laser field, the radiation pressure force will couple the two end mirrors, always creating one soft (unstable) and one hard (stable) mode [11]. This sets a lower limit on the required angular control bandwidth, which inevitably results in higher noise contamination by angular control noise and limits the angular control performance in the first and second generation gravitational-wave interferometers [27, 33, 34, 35]. Angular optical trapping can bypass the Sidles-Sigg instability. Its fundamental noise limit is quantum radiation pressure noise, making it a promising candidate for low-noise angular control.

5.2 Optical Springs

In a previous paper, we have derived the behavior of a single optical spring.

$$K_{OS} \approx P_0 t_1^2 \frac{8k}{c(1-r_1 r_2)^3} \frac{\frac{\delta}{\gamma}}{(1+\frac{\delta^2}{\gamma^2})} \frac{1}{1+\frac{\delta^2}{\gamma^2}-\frac{\Omega^2}{\gamma^2}+i2\frac{\Omega}{\gamma}} \tag{5.1}$$

In the appendix, we demonstrate the optical spring behavior of a folded cavity optical spring.

$$K_{OS} \approx P_0 t_1^2 \frac{32k}{c(1-(r_1 r_2)^2)^3} \frac{\frac{\delta}{\gamma}}{(1+\frac{\delta^2}{\gamma^2})} \frac{1}{1+\frac{\delta^2}{\gamma^2}-\frac{\Omega^2}{\gamma^2}+i2\frac{\Omega}{\gamma}} \tag{5.2}$$

This thing may not be quite right, but that's what we're looking for.

We expect some crossover from one optical spring to the other, though we have attempted to minimize this though our choice of spot locations on the mirror (see appendix A).

5.3 Setup

Our experiment (see fig. 30) uses a 1064 nm Nd:YAG laser. The laser beam is split into a carrier beam and a subcarrier beam, then the subcarrier is frequency shifted by a tunable amount, described in more detail in section IV of our previous paper [**?**]. The two beams are mode matched and spatially recombined (in opposite linear

polarizations) in a Mach-Zehnder-style setup. The recombined beam is then split using an unpolarized beamsplitter into main and side beams. The main beam enters the straight cavity, while the side beam enters the folded cavity. Both polarizations of both beams are monitored in transmission and reflection.

Parameter	Straight	Folded
λ_0	1064 nm	1064 nm
Mirror1,3,4 RoC	7.5 cm	7.5 cm
Mirror2 RoC	5.0 cm	5.0 cm
L_0	10.0 cm	20.0 cm
M1,3,4 Spot size	268 μm	268 μm
M2 Spot size	155 μm	155 μm
FSR	1.50 GHz	0.75 GHz
Finesse	7500	3750
Cavity Pole	98.6 KHz	98.6 KHz
Folded cavity angle, θ	11 deg	

δf_C	213-290 KHz
δf_{SC}	27-36 KHz
P_C input	225-239 mW
P_{SC} input	65-78 mW

Table 6 : RIGHT TABLE IS NONSENSE.

5.4 Appendix

To determine the behavior of a folded optical spring, we can compare it to the standard optical spring derivation [12].

We begin with a folded cavity with three mirrors, shown in fig. 31. We assume that M3 and M4 have the same amplitude reflectivity as M1, r_1, while we allow the end mirror to have a different reflectivity, r_2. The incoming field is $E = e^{\frac{i2\pi ct}{\lambda}}$. The average round-trip path length is $L = 2L_0$, where L_0 is the optical patch length between mirrors M3 and M4. We consider microscopic changes in cavity length d_n, which are discreet samples of a harmonic oscillation $d(t) = x_0 e^{i\Omega t}$. The light travel time between M3 and M4 is $\tau = \frac{L_0}{c}$. It is important to note that the cavity length L_0 of the folded cavity is twice that of the straight cavity in our experiment.

We can use the same X and Y notation as the original derivation with one small change. $Y = e^{-i\Omega 2\tau}$ is the same, but now $X = (r_1 r_2)^2 e^{\frac{-i2\pi L}{\lambda}}$ because the optical path touches M3 and M4 once and M2 twice.

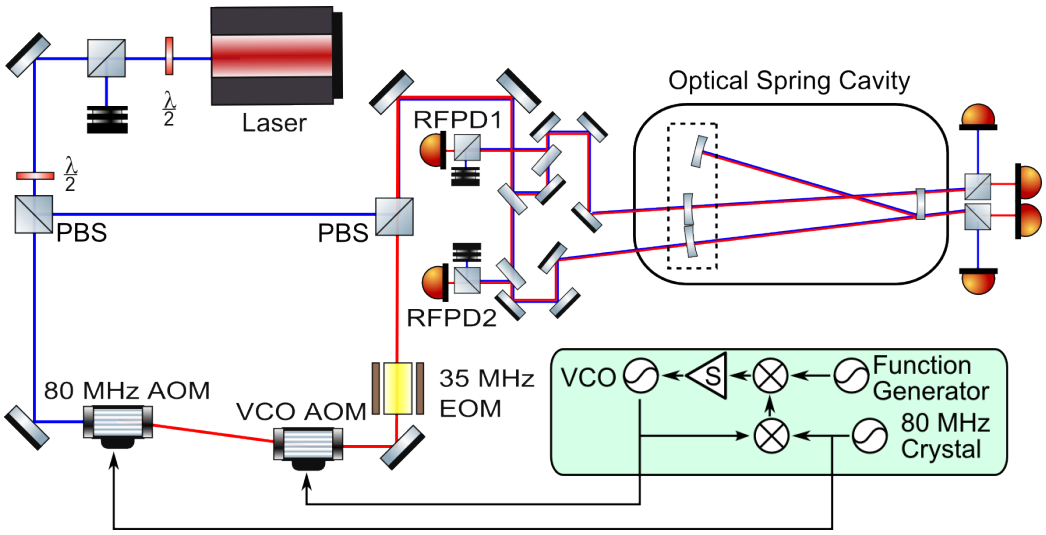

Figure 30 : Layout of the angular trap cavity experiment. The light from the laser is split into the carrier and subcarrier paths with a polarizing beam splitter (PBS), with a ratio determined by the $\lambda/2$ plate. The subcarrier path is frequency shifted by two AOMs under the control of the subcarrier servo then recombined with the carrier with another PBS. The co-aligned mode-matched beams are then split into main and side paths, which enter the trap cavity. The main beam has a straight optical path and is read out in transmission by broadband photodiodes and in reflection by RFPD1. The side beam has a folded optical path and is read out in transmission by broadband photodiodes and in reflection by RFPD2. We can use the 35 MHz modulation from the EOM with the two RFPDs in a PDH scheme to read out the cavity lengths or lock the cavities.

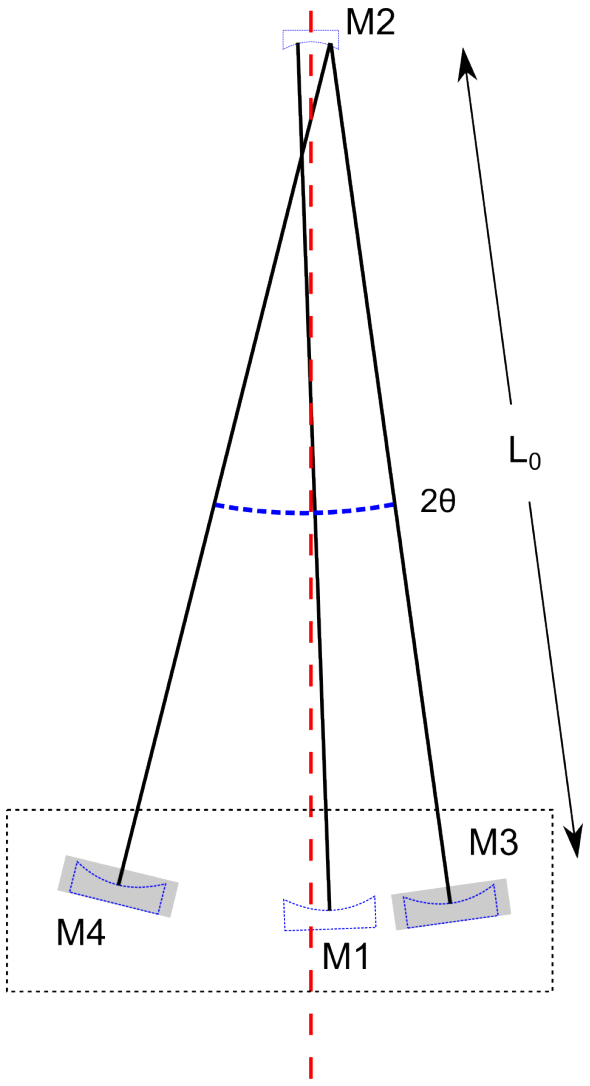

Figure 31 : Layout of the angular trap cavity. Light enters through mirrors M1 and M3. The angle θ of the folded cavity is measured from the normal of M1.

We consider a set of displacements d_n, discretely sampled from a continuously oscilating function. This is equivelent to driving the cavity length at angular frequency Ω.

$$d(t) = x_0 e^{i\Omega(t-(2n-1)\tau)} \tag{5.3}$$

$$d_1 = x_0 e^{i\Omega(t-\tau)} \tag{5.4}$$

$$d_n = Y^{2n-2} d_1 \tag{5.5}$$

Following [12], we get an equation for the electric field in the cavity, which we must change to reflect that we can only have real values for d_1.

$$E_{tot} = \frac{t_1 E}{1-X}\left[1 - \frac{4i\pi d_1}{\lambda}\frac{X}{1-Y^2X}\right]$$

$$E_{tot} = \frac{t_1 E}{1-X}\left[1 - \frac{4i\pi}{\lambda}\left(\frac{d_1}{1-Y^2X} + \frac{\overline{d}_1}{1-\overline{Y}^2X}\right)\right] \tag{5.6}$$

Then we get the cavity power:

$$P = E_{tot}\cdot\overline{E}_{tot} = P_0 t^2\left[\frac{i2\pi Y}{\lambda(1-X)(1-\overline{X})}\left(\frac{X}{1-Y^2X} - \frac{\overline{X}}{1-Y^2\overline{X}}\right)\delta L + cc\right] \tag{5.7}$$

We add an extra $Y^{1/2}$ term to get to the other side of the cavity. It is important to note that the change in cavity length δL used here is strictly that: the cavity length. If we want to transpose that into longitudinal change, we need to multiply by a geometric factor (see fig. 31):

$$\delta L = \frac{2\delta z}{\mathrm{Cos}(\theta)} \tag{5.8}$$

There is similarly a geometric correction when calculating the radiation pressure force F_{rad}

$$F_{rad} = \frac{2r_2^2}{c}P(2\mathrm{Cos}(\theta)) = K_z\delta z \tag{5.9}$$

$$= \frac{2r_2^2}{c}(2\mathrm{Cos}(\theta))P_0 t^2\left[\frac{i2\pi Y^{3/2}}{\lambda(1-X)(1-\overline{X})}\left(\frac{X}{1-Y^2X} - \frac{\overline{X}}{1-Y^2\overline{X}}\right)\frac{2\delta z}{\mathrm{Cos}(\theta)} + cc\right] \tag{5.10}$$

thus

$$K_z = \frac{4r_2^2}{c} P_0 t^2 \frac{i4\pi Y^{3/2}}{\lambda(1-X)(1-\overline{X})} \left(\frac{X}{1-Y^2X} - \frac{\overline{X}}{1-Y^2\overline{X}} \right) \tag{5.11}$$

With detuning:

$$X \to X = (r_1 r_2)^2 e^{-i2\delta\tau} \tag{5.12}$$

Here $\delta = \omega_0 - \omega_{res}$, the angular frequency detuning from the cavity resonance, $\omega_{res} = 2\pi nc/L$, and ω_0 is the frequency of the laser.

$$\begin{aligned} K_{OS} = \quad & -P_0 t^2 r_2^2 \frac{16i\pi e^{-\frac{3}{2}i\Omega\tau}}{\lambda c(1-(r_1r_2)^2 e^{i2\delta\tau})(1-(r_1r_2)^2 e^{-i2\delta\tau})} \times \\ & \left(\frac{(r_1r_2)^2 e^{-i\delta\tau}}{1-(r_1r_2)^2 e^{-2i\Omega\tau} e^{-i2\delta\tau}} - \frac{(r_1r_2)^2 e^{i2\delta\tau}}{1-(r_1r_2)^2 e^{-2i\Omega\tau} e^{i2\delta\tau}} \right) \end{aligned} \tag{5.13}$$

Considering the finesse for the folded cavity to be $F = \pi \frac{FSR}{\gamma} \approx \frac{\pi}{1-(r_1r_2)^2}$

keep in mind that we have half the FSR of a non-folded cavity and half the finesse, so γ is the same here as it is for the longitudinal trap.

$$K_{OS} \approx P_0 t_1^2 \frac{32k}{c(1-(r_1r_2)^2)^3} \frac{\frac{\delta}{\gamma}}{(1+\frac{\delta^2}{\gamma^2})} \frac{1}{1+\frac{\delta^2}{\gamma^2} - \frac{\Omega^2}{\gamma^2} + i2\frac{\Omega}{\gamma}} \tag{5.14}$$

This is important because it means that a folded cavity angular spring will behave differently. Namely, the folded cavity spring constant is four times larger in magnitude than a similar straight cavity.

5.4.1 angular issues

worried about the change in beam shape not an issue (but did lock on TEM01)

shape of power distribution on end mirror.

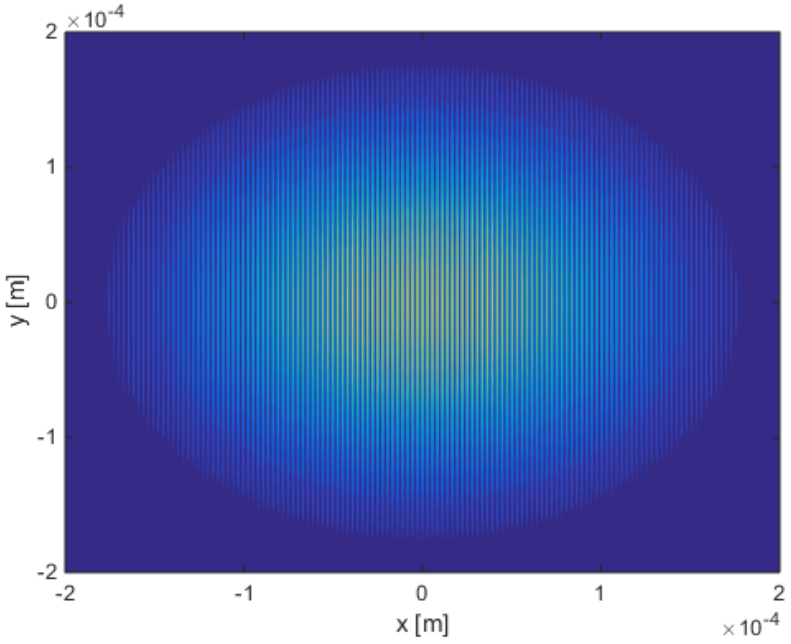

Figure 32 : Simulated folded cavity interference pattern on the surface of M2. This corresponds to the power deposited into the mirror and thus the amplitude of the photothermal effect. Using this and the diffusion length as a function of frequency, we showed that there would be no significant amplification of the photothermal effect due to this distribution of absorbed power.

Chapter 6

Application

6.1 What we're dealing with

Angular control in LIGO is an important contribution to the noise budget at the frequencies of highest sensitivity. (T0900511)

There are four different angular modes for the two Fabry-Perot arms in the LIGO interferometer, shown in figure 33. The two Hard modes are stable as the power increases, which means that the radiation pressure will push the mirrors back to an equilibrium position. The two Soft modes are unstable as the power increases, pushing the mirrors away from equilibrium.

Angular noise can couple in to differential arm length (DARM) though the interaction between beam spot motion (BSM) and angular motion (θ) on mirrors. This happens in two ways: both a static offset in the BSM with mirror angular noise and a static angular offset with BSM noise can create DARM noise.

$$\hat{\Delta L}(f) = \hat{d}_{spot}(f) * \hat{\theta}_{Mirror}(f) \approx \hat{d}_{spot}(f) * \theta^{RMS}_{Mirror}(f) + d^{RMS}_{spot}(f) * \hat{\theta}_{Mirror}(f) \quad (6.1)$$

Barsotti and Evans showed that, in Science Mode, angular noise from Common Soft and Differential Soft (the two modes of the arms that are unstable at high power) contribute the most to DARM noise.

Using angular trapping methods, we can reduce part of this noise contribution by damping the angular motion $\hat{\theta}_{Mirror}(f)$.

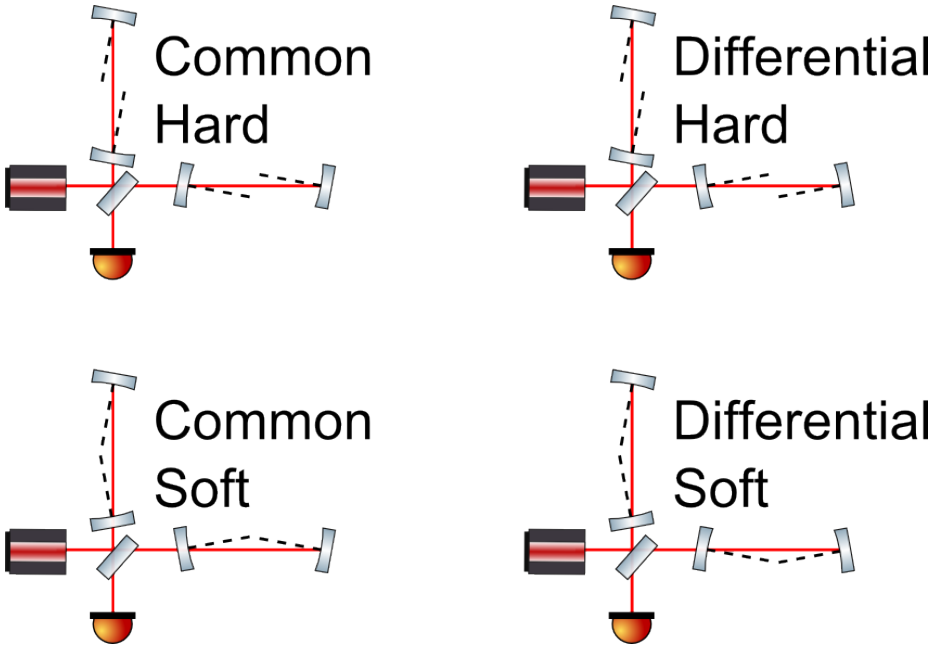

Figure 33 : The four modes of the Fabry-Perot cavities in LIGO. The two hard modes are stable and the two soft modes are unstable.

6.2 Applying angular control

For our discussion, we will disregard the distinction between common and differential modes of the interferometer.

I have considered two possible options that could (with some effort) be implemented in a LIGO-style interferometer.

6.2.1 Local damping

Damping relative to something very heavy in the end station

BSC4 layout: D0901154

Pros:

- Can keep the same ETM/ITM suspensions
- Modular: easy to modify and/or disable
- Easier to build, align and lock
- Affects Soft and Hard modes equally.

Cons:

- Different parameters for ETM and ITM
- Folded Cavities
- worry about ISI weight limit

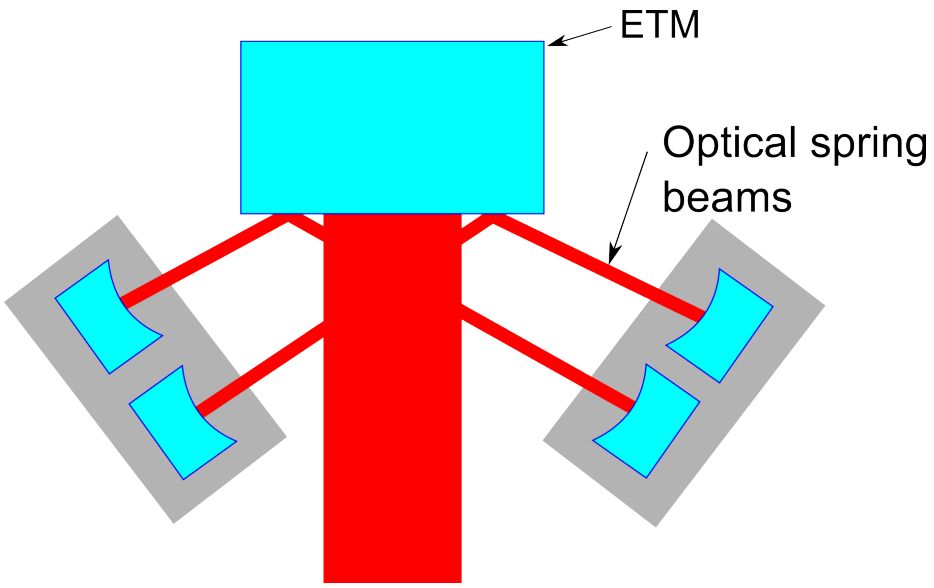

Figure 34 : Diagram of a local angular control scheme. This relies on the small mirrors being mounted in something heavier than the test mass.

In this design, we use radiation pressure to couple e.g. the ETM (about 40 kg) to two much larger masses (about 400 kg each) made out of stainless steel. In this fashion, we can damp the angular motion of the test mass relative to the hopefully much more stable masses on the side.

6.2.2 4 km damping

Damping ETM relative to ITM. This will have significant changes because the masses of the ETM and ITM are currently the same. The angular trap we have damps the motion of one mirror by pushing on the other. In a system with equal masses, this just couples the mirrors, it doesn't damp.

Pros:

Parameter	**Metric**
Cavity length, L	2 m
ETM power transmission, $T2$	5 ppm
ETM $r2$	0.9999975
ETM Diameter D	34 cm
ETM Thickness t	20 cm
Side diameter D_s	48 cm
Side thickness t_s	30 cm
Side ROC	1.5 m
Cavity FSR	75 MHz

Table 7 : Characteristics of proposed local angular design

Parameter	**Metric**
Carrier Power P_c	10 W
Subcarrier Power P_s	2 W
Carrier Detuning df_c	9000 Hz
Subcarrier Detuning df_s	-2500 Hz
OS Angle θ	45 deg

Table 8 : Characteristics of proposed local angular optical spring

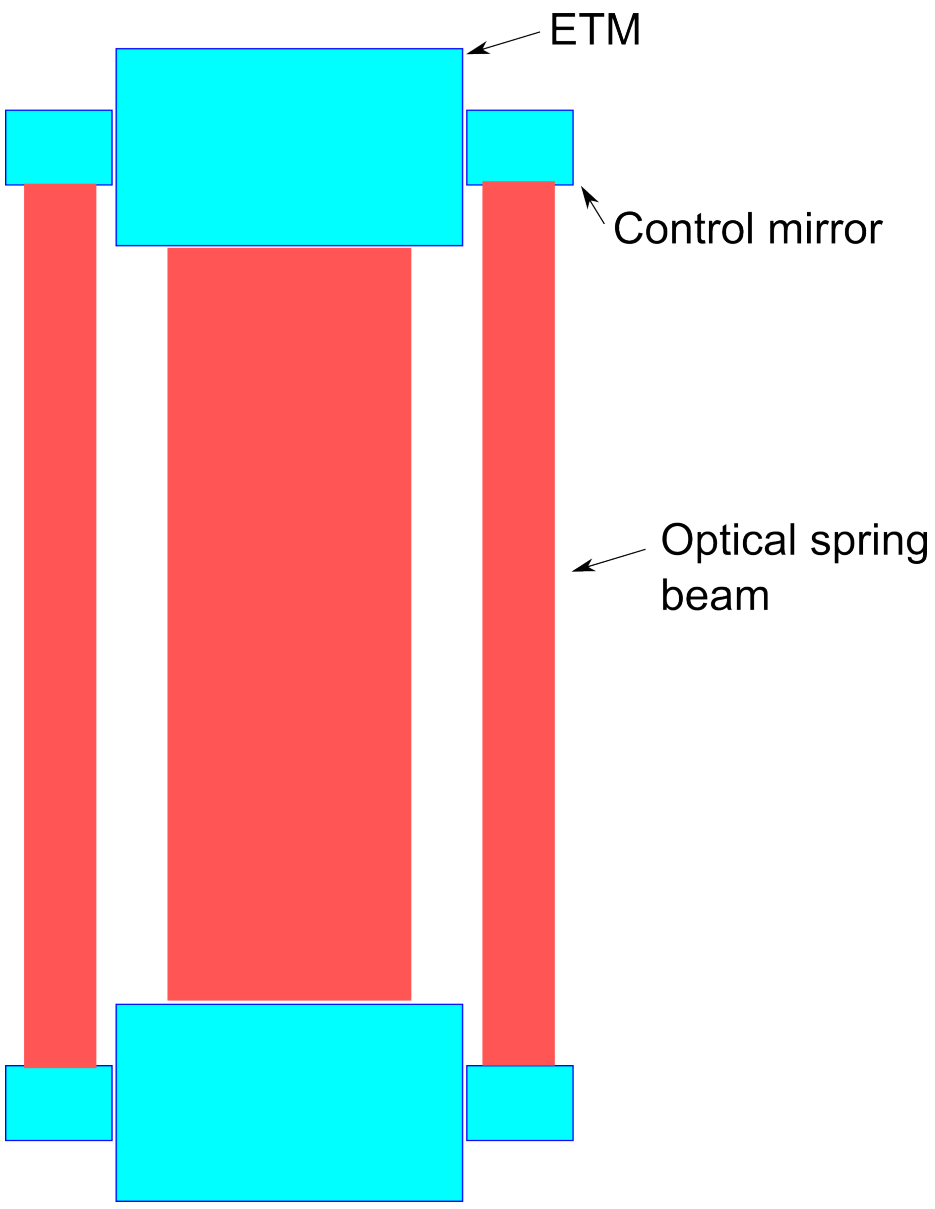

Figure 35 : Diagram of a 4km angular control scheme. This relies on control mirrors attached to the side of the test mass.

- Straight cavities
- Lower vacuum chamber volume
- Damp only Soft mode

Cons:

- Does not see Hard mode motion of cavity
- Modify test masses and probably suspensions
- Hard/risky to adjust

Parameter	**Metric**
Cavity length, L	3994.5 m
ITM power transmission, $T1$	1.4%
ETM power transmission, $T2$	5 ppm
ITM $r1$	0.99298
ETM $r2$	0.9999975
Cavity FSR	37.52 KHz

Table 9 : Characteristics of proposed long angular design

6.3 noise benefits

The cool thing about this method is that it can work independently and in tandem with existing control systems.

6.4 path to angular damping with optical springs in aLIGO

I think we might want to get rid of this section.

Chapter 7

Conclusion

I hope to have found something by this point in the thesis.

Appendix A

Beam Separation

A.1 Definitions

- P_m Input power of the main beam
- P_s Input power of the side beam
- f_m Main cavity finesse
- f_s Side cavity finesse
- R_c Radius of curvature of payload mirror (5 cm)
- θ_m Main beam angle from optical axis. Origin is at center of curvature.
- θ_s Side beam angle from optical axis. Origin is at center of curvature.
- c Speed of light
- R Payload mirror radius
- h Payload mirror thickness
- m Payload mirror mass
- $I = \frac{m}{12}(3R^2 + h^2)$ Payload mirror moment of inertia
- $G = \frac{P_m f_m}{P_s f_s}$ Handy constant
- $d = \theta_m R_c - \theta_s R_c$ Beam spot seperation

A.2 Balancing torques

We want the mirror to be stationary, so the net torque on the mirror should be zero.

Force on payload mirror due to radiation pressure of the two beams:

$$F_m = \frac{2P_m f_m}{c} \qquad F_s = \frac{2P_s f_s}{c}$$

$$\tau = F_m \theta_m R_c + F_s \theta_s R_c = 0$$

substituting in d,

$$\theta_m = \frac{d}{R_c(1+G)}$$

A.3 Eliminating beam coupling

We propose that there is a spot somewhere on the surface of the payload mirror where the sum of torque and force due to one beam makes the net force zero. We place one beam spot at r_1. We'd like to put the other beam in the null spot r_2 so that there is no force coupling between the two.

$$Fs = \frac{2P_s f_s}{c} = m\omega^2 x \qquad x = \frac{F_s}{m\omega^2}$$
$$\tau_s = F_s r_1 = I\omega^2 \phi \qquad \phi = \frac{F_s r_1}{I\omega^2}$$

Let's find a point these effects cancel:

$$r_2\phi - x = 0 \qquad r_2 = \frac{x}{\phi} = \frac{I}{mr_1}$$

It should be noted that the previously used d can also be expressed as $d = r_2 - r_1$.

$$r_2 = \theta_2 R_c = \theta_m R_c$$

$$r_2 = \frac{d}{1+G}$$

$$\frac{I}{m} = \frac{(r_2 - r_1)r_1}{1+G} = \frac{\left(\frac{I}{mr_1} + r_1\right) r_1}{1+G}$$

$$r_1 = \sqrt{\frac{I}{mG}} \qquad r_2 = \sqrt{\frac{IG}{m}}$$

These radii are the ideal horizontal distances from the payload mirror optical axis to the beam spots.

Bibliography

[1] M. Evans, S. Ballmer, M. Fejer, P. Fritschel, G. Harry, and G. Ogin. Thermo-optic noise in coated mirrors for high-precision optical measurements. *Phys. Rev. D*, 78:102003, Nov 2008.

[2] M. M. Fejer, S. Rowan, G. Cagnoli, D. R. M. Crooks, A. Gretarsson, G. M. Harry, J. Hough, S. D. Penn, P. H. Sneddon, and S. P. Vyatchanin. Thermoelastic dissipation in inhomogeneous media: loss measurements and displacement noise in coated test masses for interferometric gravitational wave detectors. *Phys. Rev. D*, 70:082003, Oct 2004.

[3] Gregory M Harry and the LIGO Scientific Collaboration. Advanced ligo: the next generation of gravitational wave detectors. *Classical and Quantum Gravity*, 27(8):084006, 2010.

[4] J. Degallaix, T. Accadia, F. Acernese, M. Agathos, A. Allocca, P. Astone, G. Ballardin, F. Barone, M. Bejger, M. G. Beker, M. Bitossi, M. A. Bizouard, M. Blom, F. Bondu, L. Bonelli, R. Bonnand, V. Boschi, L. Bosi, B. Bouhou, C. Bradaschia, M. Branchesi, T. Briant, A. Brillet, V. Brisson, T. Bulik, H. J. Bulten, D. Buskulic, C. Buy, G. Cagnoli, E. Calloni, B. Canuel, F. Carbognani, F. Cavalier, R. Cavalieri, G. Cella, E. Cesarini, E. Chassande-Mottin, A. Chincarini, A. Chiummo, F. Cleva, E. Coccia, P.-F. Cohadon, C. N. Colacino, A. Colla, M. Colombini, A. Conte, J.-P. Coulon, E. Cuoco, S. D'Antonio, V. Dattilo, M. Davier, R. Day, R. De Rosa, G. Debreczeni, W. Del Pozzo, L. Di Fiore, A. Di Lieto, A. Di Virgilio, A. Dietz, M. Drago, G. Endroczi, V. Fafone, I. Ferrante, F. Ferrini, F. Fidecaro, I. Fiori, R. Flaminio, L. A. Forte, J.-D. Fournier, J. Franc, S. Franco, S. Frasca, F. Frasconi, M. Galimberti, L. Gammaitoni, F. Garufi, M. E. Gáspár, G. Gemme, E. Genin, A. Gennai, A. Giazotto, R. Gouaty, M. Granata,

G. M. Guidi, A. Heidmann, H. Heitmann, P. Hello, G. Hemming, P. Jaranowski, R. J. G. Jonker, M. Kasprzack, I. Kowalska, A. Królak, N. Leroy, N. Letendre, T. G. F. Li, M. Lorenzini, V. Loriette, G. Losurdo, E. Majorana, I. Maksimovic, V. Malvezzi, N. Man, M. Mantovani, F. Marchesoni, F. Marion, J. Marque, F. Martelli, A. Masserot, J. Meidam, C. Michel, L. Milano, Y. Minenkov, M. Mohan, N. Morgado, S. Mosca, B. Mours, L. Naticchioni, I. Neri, F. Nocera, L. Palladino, C. Palomba, F. Paoletti, R. Paoletti, M. Parisi, A. Pasqualetti, R. Passaquieti, D. Passuello, M. Pichot, F. Piergiovanni, L. Pinard, R. Poggiani, G. A. Prodi, M. Punturo, P. Puppo, D. S. Rabeling, I. Rácz, P. Rapagnani, V. Re, T. Regimbau, F. Ricci, F. Robinet, A. Rocchi, L. Rolland, R. Romano, Rosiń, D. ska, P. Ruggi, E. Saracco, B. Sassolas, D. Sentenac, L. Sperandio, R. Sturani, B. Swinkels, M. Tacca, L. Taffarello, A. P. M. ter Braack, A. Toncelli, M. Tonelli, O. Torre, E. Tournefier, F. Travasso, G. Vajente, J. F. J. van den Brand, C. Van Den Broeck, S. van der Putten, M. Vasuth, M. Vavoulidis, G. Vedovato, D. Verkindt, F. Vetrano, A. Viceré, J.-Y. Vinet, S. Vitale, H. Vocca, R. L. Ward, M. Was, M. Yvert, A. Zadrożny, and J.-P. Zendri. Advanced Virgo Status. In G. Auger, P. Binétruy, and E. Plagnol, editors, *9th LISA Symposium*, volume 467 of *Astronomical Society of the Pacific Conference Series*, page 151, January 2013.

[5] Kentaro Somiya. Detector configuration of KAGRA: The Japanese cryogenic gravitational-wave detector. *Class.Quant.Grav.*, 29:124007, 2012.

[6] V.B. Braginsky, M.L. Gorodetsky, and S.P. Vyatchanin. Thermo-refractive noise in gravitational wave antennae. *Physics Letters A*, 271(56):303 – 307, 2000.

[7] M. Cerdonio, L. Conti, A. Heidmann, and M. Pinard. Thermoelastic effects at low temperatures and quantum limits in displacement measurements. *Phys. Rev. D*, 63:082003, Mar 2001.

[8] V.B. Braginsky, M.L. Gorodetsky, and S.P. Vyatchanin. Thermodynamical fluctuations and photo-thermal shot noise in gravitational wave antennae. *Physics Letters A*, 264(1):1 – 10, 1999.

[9] M. De Rosa, L. Conti, M. Cerdonio, M. Pinard, and F. Marin. Experimental measurement of the dynamic photothermal effect in fabry-perot cavities for gravitational wave detectors. *Phys. Rev. Lett.*, 89:237402, Nov 2002.

[10] Stefan W. Ballmer. Photothermal transfer function of dielectric mirrors for precision measurements. *Phys. Rev. D*, 91:023010, Jan 2015.

[11] J.A. Sidles and D. Sigg. Optical torques in suspended fabryperot interferometers. *Phys. Lett. A*, 354(3):167 – 172, 2006.

[12] A. Perreca, J. Lough, D. Kelley, and S. W. Ballmer. Multidimensional optical trapping of a mirror. *Phys. Rev. D*, 89(12):122002, June 2014.

[13] Thomas Corbitt, Yanbei Chen, Edith Innerhofer, Helge Müller-Ebhardt, David Ottaway, Henning Rehbein, Daniel Sigg, Stanley Whitcomb, Christopher Wipf, and Nergis Mavalvala. An all-optical trap for a gram-scale mirror. *Phys. Rev. Lett.*, 98:150802, 2007.

[14] James Lough. *Optical Spring Stabilization*. PhD thesis, Syracuse University, 2014. Dissertations - ALL. Paper 172.

[15] D. Heinert, K. Craig, H. Grote, S. Hild, H. Lück, R. Nawrodt, A. Simakov, D. V. Vasilyev, D. P. Vyatchanin, S. and H. Wittel. Thermal noise of folding mirrors. *Phys. Rev. D*, 90:042001, Aug 2014.

[16] B. S. Sheard, M. B. Gray, C. M. Mow-Lowry, D. E. McClelland, and S. E. Whitcomb. Observation and characterization of an optical spring. *Phys. Rev. A*, 69(5):051801, 2004.

[17] E. D. Black. An introduction to Pound-Drever-Hall laser frequency stabilization. *Am. J. Phys.*, 69:79–87, 2001.

[18] S. W. Ballmer and D. J. Ottaway. New class of optical beams for large baseline interferometric gravitational wave detectors. *Phys. Rev. D*, 88(6):062004, 2013.

[19] B. P. Abbott, R. Abbott, R. Adhikari, P. Ajith, B. Allen, G. Allen, R. S. Amin, S. B. Anderson, W. G. Anderson, M. A. Arain, and et al. LIGO: the Laser

Interferometer Gravitational-Wave Observatory. *Rep. Prog. Phys.*, 72(7):076901, 2009.

[20] J. R. Smith and LIGO Scientific Collaboration. The path to the enhanced and advanced LIGO gravitational-wave detectors. *Classical Quantum Gravity*, 26(11):114013, 2009.

[21] G. M. Harry and LIGO Scientific Collaboration. Advanced LIGO: the next generation of gravitational wave detectors. *Classical and Quantum Gravity*, 27(8):084006, April 2010.

[22] Giovanni Losurdo. Ground-based gravitational wave interferometric detectors of the first and second generation: an overview. *Classical Quantum Gravity*, 29(12):124005, 2012.

[23] C. M. Caves. Quantum-Mechanical Radiation-Pressure Fluctuations in an Interferometer. *Phys. Rev. Lett.*, 45:75–79, 1980.

[24] W.-T. Ni. Quantum measurements and the standard quantum limit. *Phys. Rev. A*, 33:2225–2229, 1986.

[25] S. L. Danilishin and F. Y. Khalili. Quantum Measurement Theory in Gravitational-Wave Detectors. *Living Rev. Relativity*, 15:5, 2012.

[26] Y. Chen. Macroscopic quantum mechanics: theory and experimental concepts of optomechanics. *J. Phys. B*, 46(10):104001, 2013.

[27] LIGO Document. Report No LIGO-T1000416-v3, 2010.

[28] V. B. Braginsky, S. E. Strigin, and S. P. Vyatchanin. Analysis of parametric oscillatory instability in power recycled LIGO interferometer. *Phys. Lett. A*, 305:111–124, 2002.

[29] O. Arcizet, T. Briant, A. Heidmann, and M. Pinard. Beating quantum limits in an optomechanical sensor by cavity detuning. *Phys. Rev. A*, 73(3):033819, 2006.

[30] T. Corbitt, D. Ottaway, E. Innerhofer, J. Pelc, and N. Mavalvala. Measurement of radiation-pressure-induced optomechanical dynamics in a suspended Fabry-Perot cavity. *Phys. Rev. A*, 74(2):021802, 2006.

[31] T. J. Kippenberg, H. Rokhsari, T. Carmon, A. Scherer, and K. J. Vahala. Analysis of Radiation-Pressure Induced Mechanical Oscillation of an Optical Microcavity. *Phys. Rev. Lett.*, 95(3):033901, 2005.

[32] M. Punturo and et al. The third generation of gravitational wave observatories and their science reach. *Classical Quantum Gravity*, 27(8):084007, 2010.

[33] V.B. Braginsky, S.E. Strigin, and S.P. Vyatchanin. Parametric oscillatory instability in FabryPerot interferometer. *Phys. Lett. A*, 287(56):331 – 338, 2001.

[34] Katherine L. Dooley, Lisa Barsotti, Rana X. Adhikari, Matthew Evans, Tobin T. Fricke, Peter Fritschel, Valera Frolov, Keita Kawabe, and Nicolás Smith-Lefebvre. Angular control of optical cavities in a radiation-pressure-dominated regime: the enhanced ligo case. *J. Opt. Soc. Am. A*, 30(12):2618–2626, 2013.

[35] Eiichi Hirose, Keita Kawabe, Daniel Sigg, Rana Adhikari, and Peter R. Saulson. Angular instability due to radiation pressure in the ligo gravitational-wave detector. *Appl. Opt.*, 49(18):3474–3484, 2010.

Curriculum Vitae

Title of Dissertation

Angular trapping of a mirror using radiation pressure

Full Name

David B. Kelley

Place and Date of Birth

Poughkeepsie, New York December 3, 1987

Colleges and Universities,	Years attended and degrees
Massachusetts Institute of Technology	2006–2010, B.S.
Syracuse University	2010–2015, Ph.D.

Publications

1. Duncan A Brown, Stanislav Babak, Patrick R Brady, Nelson Christensen, Thomas Cokelaer, Jolien D E Creighton, Stephen Fairhurst, Gabriela Gonzalez, Eirini Messaritaki, B S Sathyaprakash, Peter Shawhan, and Natalia Zotov, *Searching for gravitational waves from binary inspirals with LIGO*, Classical and Quantum Gravity **21** S1625–S1633 (2004)

2. Abbott B et al., *First upper limits from LIGO on gravitational wave bursts*, Phys Rev **D69** 102001 (2004)

3. Abbott B et al., *Analysis of first LIGO science data for stochastic gravitational waves*, Phys Rev **D69** 122004 (2004)

4. Abbott B et al., *Analysis of LIGO data for gravitational waves from binary neutron stars*, Phys Rev **D69** 122001 (2004)

5. Brown Duncan A, *Testing the LIGO inspiral analysis with hardware injections*, Class Quant Grav **21** S797–S800 (2004)

6. Abbott B et al., *Setting upper limits on the strength of periodic gravitational waves using the first science data from the GEO 600 and LIGO detectors*, Phys Rev **D69** 082004 (2004)

7. Abbott B et al., *Detector description and performance for the first coincidence observations between LIGO and GEO*, Nucl Instrum Meth **A517** 154–179 (2004)

Awards and Fellowships

2010 Fellowship??

Major Department

Physics